Atomic scale control and understanding of cubic silicon carbide surface reconstructions, nanostructures and nanochemistry

2004 J. Phys.: Condens. Matter 16 S1611

(http://iopscience.iop.org/0953-8984/16/17/011)

INSTITUTE OF PHYSICS PUBLISHING JOURNAL OF PHYSICS: CONDENSED MATTER

J. Phys.: Condens. Matter **16** (2004) S1611–S1658 PII: S0953-8984(04)77040-X

Atomic scale control and understanding of cubic silicon carbide surface reconstructions, nanostructures and nanochemistry

Patrick G Soukiassian and Hanna B Enriquez

Commissariat à l'Energie Atomique, Laboratoire SIMA Associé à l'Université de Paris-Sud/Orsay, DSM-DRECAM-SPCSI, Saclay, Bâtiment 462, 91191 Gif sur Yvette Cedex, France

Received 4 March 2004
Published 16 April 2004
Online at stacks.iop.org/JPhysCM/16/S1611
DOI: 10.1088/0953-8984/16/17/011

Abstract

The atomic scale ordering and properties of cubic silicon carbide (β-SiC) surfaces and nanostructures are investigated by atom-resolved room and high-temperature scanning tunnelling microscopy (STM) and spectroscopy (STS), synchrotron radiation-based valence band and core level photoelectron spectroscopy (VB-PES, CL-PES) and grazing incidence x-ray diffraction (GIXRD). In this paper, we review the latest results on the atomic scale understanding of (i) the structure of β-SiC(100) surface reconstructions, (ii) temperature-induced metallic surface phase transition, (iii) one dimensional Si(C) self-organized nanostructures having unprecedented characteristics, and on (iv) nanochemistry at SiC surfaces with hydrogen. The organization of these surface reconstructions as well as the 1D nanostructures' self-organization are primarily driven by surface stress. In this paper, we address such important issues as (i) the structure of the Si-rich 3×2, the Si-terminated c(4×2), the C-terminated c(2×2) reconstructions of the β-SiC(100) surface, (ii) the temperature-induced reversible c$(4 \times 2) \Leftrightarrow 2 \times 1$ metallic phase transition, (iii) the formation of highly stable (up to 900 °C) Si atomic and vacancy lines, (iv) the temperature-induced sp to sp^3 diamond like surface transformation, and (v) the first example of H-induced semiconductor surface metallization on the β-SiC(100) 3×2 surface. The results are discussed and compared to other experimental and theoretical investigations.

(Some figures in this article are in colour only in the electronic version)

1. Introduction and historical background

Silicon carbide (SiC) has been known for nearly two centuries since its existence was predicted in the early 19th century in Linköping (Sweden) by Berzelius [1]. At the end of the 19th century, Acheson in Pittsburgh, Pennsylvania (USA) was able to synthesize SiC, then known

as 'carborundum' [2]. However, SiC is a much older material since it is even older than the solar system. Indeed, a few years later (1895) a French pharmacist, Henri Moisan (1904 Chemistry Nobel Prize laureate) discovered SiC on a meteorite located in the Diablo Canyon (Arizona) [3]. Then, for many years, SiC was known for its outstanding mechanical properties and was primarily used as a hard material (the highest hardness after those of diamond and boron nitride). SiC now became very well known as an advanced and versatile material having many existing and promising applications in matrix composites, biocompatibility or microelectronics [4–6]. In the latter field, SiC appears to be especially suitable for high-power, high-temperature, high-voltage, high-frequency and radiation-resistant electronic devices and sensors [4–6]. Its average figures of merit scale up to three orders of magnitude, well above those of conventional semiconductors such as Si or III–V compounds, SiC being outclassed only by diamond [7–9]. Furthermore, SiC is chemically rather inert which, combined with its ability to resist radiation damage, makes it a very suitable material for harsh environments [6, 9]. SiC is a 'refractory' IV–IV compound semiconducting material belonging to the class of wide band gap semiconductors (together with diamond and group III nitrides) with a very high thermal stability [4–9]. This makes it very useful for operations at elevated temperatures ($\geqslant$600–800 °C instead of $<$150 °C e.g. for silicon) [4–9]. Overall, these characteristics give to SiC many potential applications in aerospace, automotive, electronics and nuclear industries [4–9]. In addition, due to a small mismatch in lattice parameters, SiC (in both cubic and hexagonal phases) is a very suitable substrate for III–V nitride epitaxial growth [4]. SiC exits in (β) cubic, (α) hexagonal (more than 170 polytypes) or rhombohedral crystallographic phases, having band gaps ranging from 2.4 to 3.3 eV, which allows the manufacture of homojunctions and superlattices based on the same material [10]. Its breakdown field, thermal conductance, band gap and saturated drift velocity are respectively $\times$10 times, $\times$3 times (the same as Cu), $\times$2 times and $\times$2 times higher than silicon [4–6, 8]. Among many other applications, figure 1 gives an example of the microwave characteristics simulated for an SiC BARITT diode compared

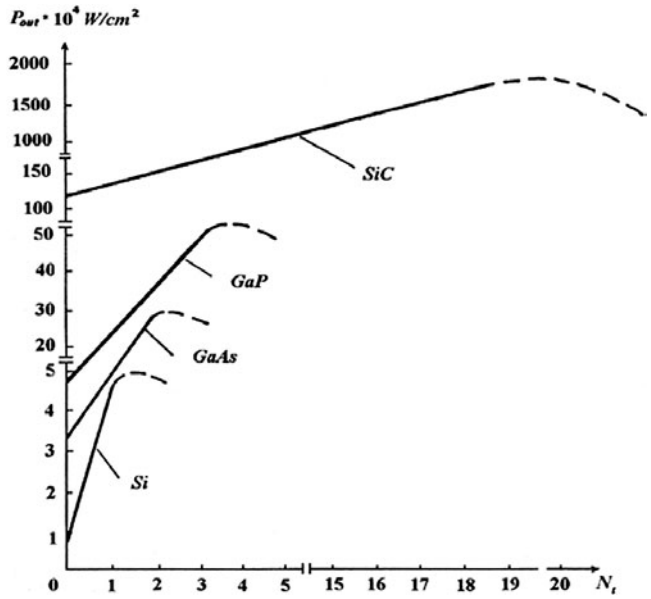

Figure 1. Maximum available microwave power as a function of the trap concentration levels N_t for various BARITT diodes based on Si, GaAs, GaP and SiC semiconductors.

with same BARITT devices made from Si and other conventional semiconductors [11]. One can clearly see from figure 1 that the microwave power performances for an SiC-based BARITT diode scale an average of about 2–3 orders of magnitude above those manufactured with other semiconducting materials [11]. SiC also seems to be a promising material as an ultraviolet sensor and for solar cells [12–14]. Due to their larger band gap compared to cubic SiC (2.9 to 3.3 eV instead of 2.4 eV), hexagonal 6H- and 4H-SiC polytypes are often preferred in high-power/high-temperature applications [4–6]. However, cubic β-SiC has a much higher carrier mobility, which makes it more suitable for high-frequency applications [4–6].

One of the major problems with SiC is the growth of high-quality single crystals. Bulk single crystal growth has been successfully achieved for the hexagonal phase (α) using the Lely [15] and the modified Lely [16] methods which have been used and significantly developed in Saint Petersburg (Russia) at the Ioffe Institute and at the Electrotechnical University, and now also in many other national laboratories, academic institutions and industrial companies worldwide [17, 18]. While large (wafers having diameters $\approx 2'$ and now $3'$) single crystal 4H-SiC and 6H-SiC wafer could be obtained, this method still leaves a significant density of micro-pipes in the bulk of the material; these have detrimental effects in device applications. The situation is much more complicated for cubic (β) SiC (or 3C-SiC) crystals for which bulk crystal growth has always resulted in high defect densities. Another approach for cubic silicon carbide crystals is the growth of SiC thin films about few 1 μm thick on an Si(100) wafer by C_3H_8 and SiH_4 chemical vapour deposition (CVD) on vicinal (4°) Si(100) wafers [19–21]. This process is now commonly used and allows us to achieve single domain β-SiC(100) thin film crystals having much lower defect densities.

From a fundamental point of view, SiC is not a fully covalent semiconductor, unlike other group IV semiconductors such as silicon, germanium or diamond, with a significant charge transfer between C and Si which, due to an underlying C layer, results in its (100) face being a polar surface. With the availability of good quality samples, the understanding and control of both cubic and hexagonal SiC surfaces and interfaces has been successfully achieved only recently, contrary to the surfaces of conventional semiconductors like, for example, Si, Ge or III–V compounds that have been investigated for several decades [22–25]. Initially, the cubic β-SiC surfaces were expected to have similar properties to those of Si or Ge. Cubic β-SiC has the zinc blende structure with alternating Si and C planes, leading for the β-SiC(100) surface to many different reconstructions ranging from Si-rich $3 \times 2, 8 \times 2, 5 \times 2, 7 \times 2, 9 \times 2, \ldots, (2n + 1) \times 2$, Si-terminated c$(4 \times 2)$ and 2×1, C-terminated c(2×2) and C-rich 1×1 graphitic surfaces, as evidenced by both experimental and theoretical investigations [4, 8, 26–46]. From this aspect, silicon carbide appears as a 'surface science laboratory' [47]. Figure 2 gives a schematic diagram of the various reconstructions of the β-SiC(100) surface.

Due to very large mismatches between lattice parameters when comparing β-SiC(100) with Si(100) (-20%) and C(100) (+22%), the Si surface plane is under very large compressive stress while the C surface plane would be, in turn, under strong stretching stress [4, 8, 28, 29, 32, 33, 38, 43, 46]. This makes silicon carbide a test case to probe the effect of stress in surface organization. Indeed, we will see below that these effects are dominant features in β-SiC(100) surface ordering. The central issue is the control, at the atomic scale, of SiC surfaces and interfaces. In addition to high-quality, well-defined surfaces, interesting features such as a semiconducting c(4×2) to metallic 2×1 phase transition has been discovered [38, 48].

In this paper, we present some of the latest investigations on the control and understanding, at the atomic level, of (i) β-SiC(100) surface reconstructions, (ii) Si(C) atomic line and nanostructure formation, on (iii) temperature-induced metallic surface phase transitions and on

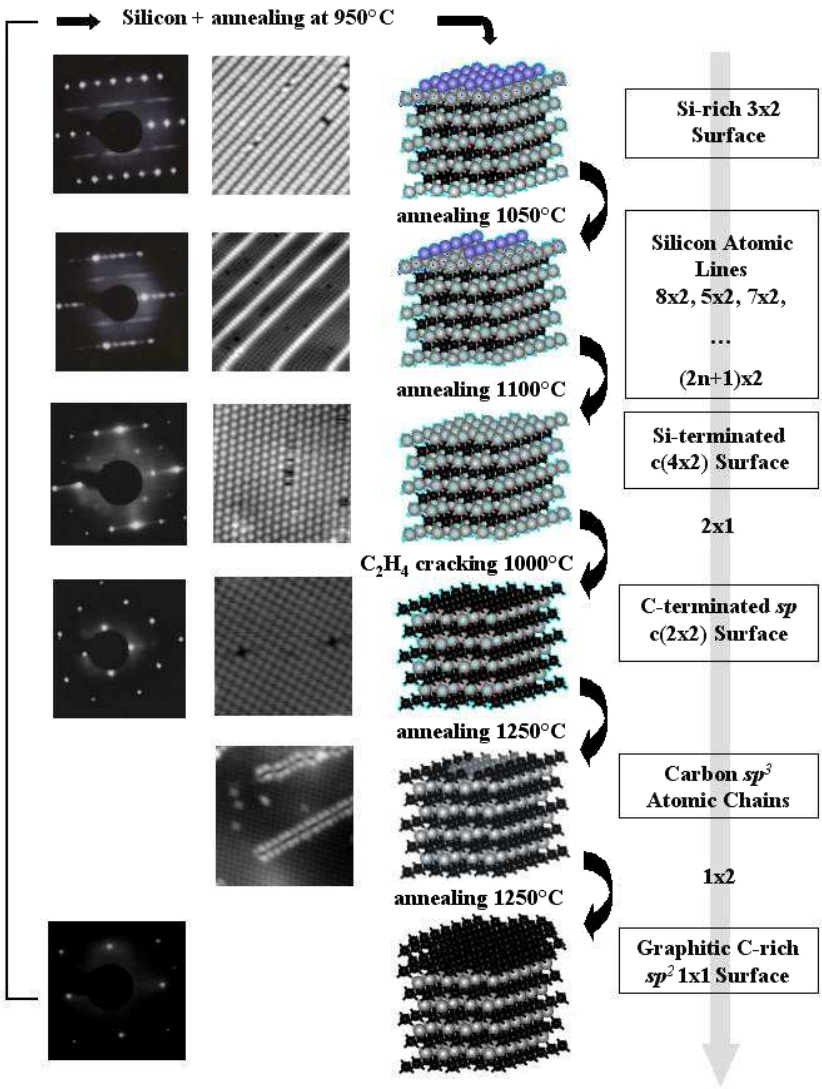

Figure 2. Schematic diagram of the β-SiC(100) surface preparation: (i) The 'as-received' β-SiC(100) is annealed above 1250 °C to remove native oxides and amorphous other carbon species, leaving a graphitic C-rich 1×1 surface. To restore the Si stoichiometry, room temperature Si deposition followed by sequences of annealing at 950 °C are performed, leading to an Si-rich 3×2 reconstruction. (ii) Selective Si removal takes place with annealing at 1050 °C leading to associated Si atomic line formation having 8×2, 5×2, 7×2, ..., $(2n + 1) \times 2$ long distance arrangements. (iii) An 1100 °C annealing removes from the surface all Si atoms in excess of 1 Si ML, leaving an Si-terminated $c(4 \times 2)$ surface reconstruction. (iv) C_2H_4 cracking at 1000 °C on the Si-terminated surface leads to a C-terminated surface (sp) having an sp $c(2 \times 2)$ surface reconstruction. (v) Annealing an sp C-terminated $c(2 \times 2)$ surface at 1250 °C leads to an sp^3 diamond-like surface with a pseudo 1×2 array. (vi) Additional annealing at 1250 °C leads to graphitization and to a 1×1 C-rich surface. The LEED diagrams are provided in the left-hand column, the STM topographs in the middle column and the schematic diagram is on the right-hand side.

(iv) some recent aspects of the nanochemistry of SiC including H-induced surface metallization. These studies are conducted on the basis of atom-resolved scanning tunnelling microscopy

(STM) and spectroscopy (STS), on synchrotron radiation-based photoelectron spectroscopies (UV-PES and XR-PES) and grazing incidence x-ray diffraction (GIXRD) techniques. Such important issues as the atomic structure, the role of stress in surface ordering and self-organized Si and C nanostructures, sp $\rightarrow$ sp^3 diamond-like temperature controlled transformation, fine details in structural changes and changes in the surface/nanostructures properties are presented. The models derived from the experimental studies are discussed and compared to available state-of-the-art *ab initio* calculations.

2. Experimental details

Since the silicon carbide surfaces could be very sensitive, all the reported experiments have been performed in ultra-high vacuum, with pressures in the experimental and preparation chambers always kept in the 10^{-11} Torr range. The STM experiments were performed using room temperature and variable temperature scanning tunnelling microscopes. The synchrotron radiation photoemission experiments were performed using the ultraviolet and soft x-ray light emitted by the 800 MeV Super ACO storage ring at Laboratoire d'Utilisation du Rayonnement Électromagnétique (LURE, Université de Paris-Sud/Orsay, France), and at the 2.4 GeV Elettra Sincrotrone (Trieste, Italy) 3rd generation storage ring. The grazing incidence x-ray diffraction experiments were performed at the 3rd generation hard x-ray 6 GeV European Synchrotron Radiation Facility (ESRF, Grenoble, France). We used single crystal, single domain β-SiC thin films ($\approx$1 μm thick) prepared at CEA-LETI (Grenoble), at the Laboratoire des Multimatériaux et Interfaces, Université Claude Bernard (Lyon) and at Centre de Recherche sur l'Hétéroépitaxie, CNRS (Sophia Antipolis) by C_3H_8 and SiH_4 chemical vapour deposition (CVD) growth on vicinal (4°) Si(100) wafers. High-quality β-SiC(100) surfaces were routinely prepared from thermal annealing sequences and Si deposition for Si-terminated surfaces. C-terminated surfaces were prepared from ethylene thermal cracking on Si-terminated surfaces. These procedures are shown to result in very reproducible and clean surfaces as confirmed by sharp single domain low-energy electron diffraction (LEED) patterns and specific electronic surface states in the valence band photoemission spectra. Figure 2 gives a schematic view of the various β-SiC(100) surface reconstructions associated with the various sequence of surface preparation, and corresponding STM topographs and LEED patterns. Additional information about high-quality β-SiC surface preparation, core level peak fitting and other experimental details can be found elsewhere [9, 27–29, 33, 34, 49].

3. Atomic ordering and properties of β-SiC(100) surface reconstructions

3.1. The morphology of the Si-rich β-SiC(100) 3 × 2 surface

We first focus on the morphology of the Si-terminated cubic β-SiC(100) 3 × 2 surface reconstruction that could be obtained from appropriate sequences of Si deposition and thermal annealing (figure 2) [8]. The native oxides (silicon dioxide and mixed Si–C oxides) and carbon/graphite clusters resulting from the MOCVD process were removed from the 'as received' β-SiC thin film surface by a thermal annealing at 1250 °C leaving a clean C-rich graphitic β-SiC(100) 1 × 1 surface [8, 51]. The 3 × 2 surface reconstruction surface was obtained by room temperature Si deposition onto a C-rich β-SiC(100) 1 × 1 surface followed by a thermal annealing at 1000 °C (figure 2). Figures 3(a)–(e) display 800 Å × 800 Å STM topographs (filled electronic states) of such a surface for various increasing Si coverages. As can be seen from these STM topographs, the surface includes several steps. Also of interest is the presence of large Si islands in figures 3(a)–(c) [32, 52]. Both islands and terraces are

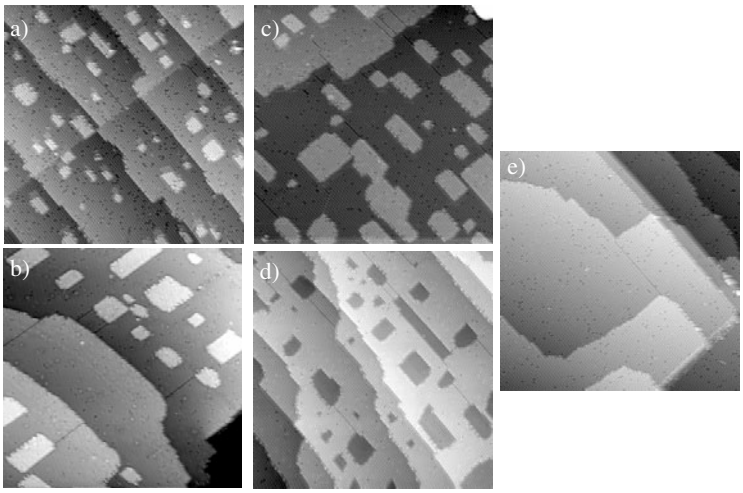

Figure 3. The morphology of the Si-rich β-SiC(100) 3×2 surface: 800 Å $\times$ 800 Å STM topographs (filled electronic states) showing (a)–(c) Si islands having a 3×2 array and (d) Si vacancy islands also having a 3×2 array, and (e) completed β-SiC(100) 3×2 surface with no Si island left. The 'electronic' height of the Si islands above the surface is 2.2 Å.

made of oval spots forming a 3×2 surface array [27]. These spots correspond to the Si–Si dimers [27]. The large Si islands, that are spread all over the terrace, result from the sequence of Si deposition followed by thermal annealings. On going from figures 3(a) to (c), one can notice that the island size increases with the sequence of Si deposition and thermal annealing, with the formation of a full terrace as can be seen at the top of figure 3(c). These Si islands and terraces are located at $\approx$2.2 Å height above the surface [27].

Figure 3(d) shows another 800 Å $\times$ 800 Å STM topograph of a 3×2 surface that was prepared using a slightly higher Si deposition resulting in a larger coverage. The surface exhibits seven steps that are all covered with vacancy islands also having a 3×2 surface array. This shows that, upon increasing the Si coverage, the Si islands observed above grow in size and coalesce to form a full terrace, leaving some vacancy islands [8, 32, 52]. At the last step (figure 3(e)), when the all surface is covered with a full Si layer, Si- or vacancy islands are no longer present on the 3×2 surface, which appears to be of high quality (comparable to silicon surfaces) with a low density of defects. The latter include some dark spots corresponding to dimer vacancies. One can also observe full dimer row vacancies that are sometimes connected to the Si islands (figures 3(b) and (c)) or to vacancy islands (figure 3(d)). The topmost Si atomic plane of the 3×2 surface reconstruction has an Si coverage of $\Theta = 1/3$ Si monolayer [8, 27, 32, 52–54].

3.2. The atomic structure of the Si-rich β-SiC(100) 3×2 surface reconstruction

3.2.1. The structure of the topmost surface atomic layer determined by atom-resolved STM: an asymmetric Si dimer row (ADR) layer. However, based on LEED, Auger, XPS and previous STM experiments, the 3×2 surface reconstruction has been interpreted to a be an Si-rich surface having an Si coverage of 2/3 of a monolayer (ML) [55–60]. From these investigations, the β-SiC(100) 3×2 surface structure was understood to result from dimer rows in which the dimer direction is parallel to the row [47, 55–60]. In contrast, medium-energy ion scattering (MEIS) and RHEED studies have shown that the Si coverage is 1/3 Si ML [47, 53, 54], with the Si dimers also being parallel to the dimer row.

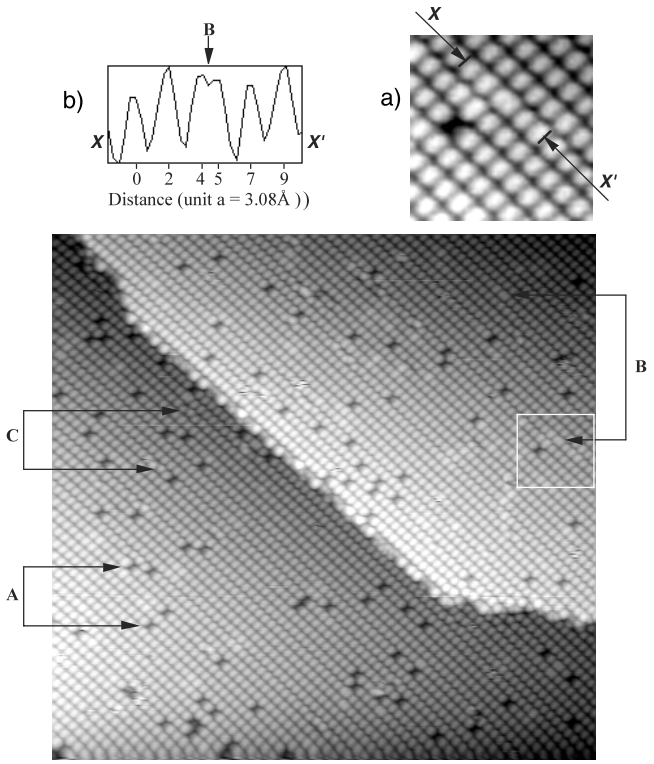

Figure 4. A β-SiC(100) 3 × 2 surface shown through a 400 Å × 400 Å STM topograph (filled electronic states). The different A, B and C types of defects mentioned in the text are marked. The tip bias was $V_t = +2.5$ V with a 0.2 nA tunnelling current. (a) Close-up of an area having type A (missing dimer) and B (dimer pair) defects. (b) Atomic profile of dimers along the XX' axis showing the two components of a dimer pair which is at the origin of an antiphase boundary, with Si dimer no longer in phase laterally.

The β-SiC(100) 3 × 2 surface structure has also been investigated by atom-resolved STM which, unlike diffraction techniques, probes the real space of the topmost surface atomic layer. Figure 4 shows a representative 400 Å × 400 Å topograph (filled electronic states) of the β-SiC(100) 3 × 2 [27]. First, one should notice the high surface quality that is comparable to Si(100) 2 × 1 with a low density of defects. The surface includes oval spots originating from individual Si–Si dimers in a 3 × 2 array and forming rows [27]. A few defects can also be seen in figure 4, including missing dimers (A), dimer pairs (B), and dimers having a different tilt angle (C). Dimer pairs are of special interest and result from two Si dimers separated by a shorter distance [27]. Figure 4(a) shows a closer view of defect B. Height profiles in figure 4(b) along the axis corresponding to the dimer rows stress better the existence of dimer pairs [27]. This defect is at the origin of dimer row translation by one times the surface lattice parameter, resulting in the formation of antiphase boundaries that can be seen in figure 4(a) [27]. Additional insights about the β-SiC(100) 3 × 2 surface structure could be found by tunnelling into the empty electronic states. Figure 5 displays such a 200 Å × 200 Å STM topograph in which the two individual Si-atoms belonging to each dimer are identified, clearly showing that the dimers are perpendicular to the row direction [27]. A height profile along the YY' axis shows that the two atoms belonging to the same dimer do not have the same height, indicating that the dimers are asymmetric [27], in qualitative agreement with *ab initio*

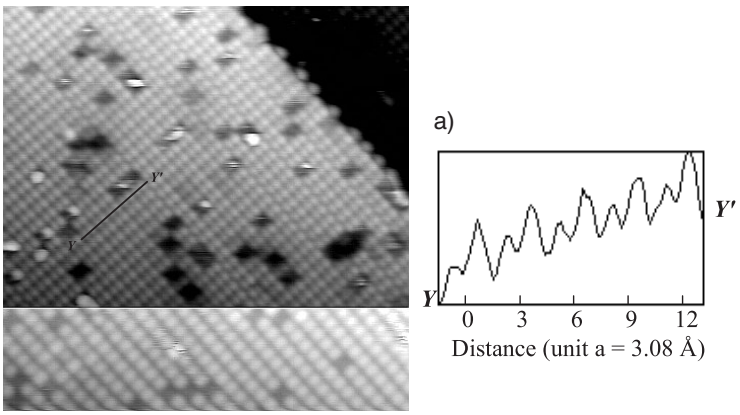

Figure 5. A β-SiC(100) 3×2 surface shown through a 200 Å $\times$ 200 Å STM topograph obtained by tunnelling into filled states (bottom) and empty states (top). The tip bias was $V_t = \pm 3.5$ V with a 0.2 nA tunnelling current. (a) Atomic profile of dimers along the YY' axis showing the height difference between two Si atoms belonging to the same dimer.

calculations [39]. Furthermore, all the dimers are seen to be tilted in the same direction, (i.e. not anticorrelated) unlike the dimers forming a c(4×2) reconstruction at low temperature on the Si(100) and Ge(100) surfaces [22, 23].

3.2.2. The structure of the whole 3×2 *surface reconstruction determined by synchrotron radiation-based grazing incidence x-ray diffraction (GIXRD): an alternately long and short dimer (ALSD) row model.* While atom-resolved STM provided the real space atomic picture of the topmost atomic layer of 3×2 surface reconstruction, this technique is basically unable to provide deep insights about the subsurface structure, i.e. to give on its own a complete structural description of the whole reconstruction. It is therefore necessary to turn to structural techniques. As mentioned above, the first observation of a 3×2 surface reconstruction was reported nearly two decades ago on the basis of LEED measurements [26, 55, 56]. To account for this periodicity, a model involving two silicon atomic planes, with a $2/3$ ML surface plane on a full silicon atomic plane, was proposed [55]. In this model, the surface dimerization leads to a $\times 2$ periodicity along the Si–Si dimers, whereas one dimer in three is missing, leading to a $\times 3$ periodicity in the perpendicular direction and to the $2/3$ ML coverage. Subsequently, two dimers are included per unit cell, so that it is called the double dimer row model (DDRM), with dimer rows parallel to the dimer direction (figure 6). But a few years later, medium-energy ion scattering (MEIS) experiments derived a $1/3$ ML coverage for the last atomic plane (instead of $2/3$) [53, 54]. On this basis, a single dimer row model (SDRM) was proposed with only one Si–Si dimer per unit cell (figure 6). One should notice that the surface dimers are parallel to the $\times 2$ direction in both DDRM and SDRM (figure 6). When the last atomic plane is removed, the underlying Si atomic plane can therefore form dimers, leading to a 2×1 or c(4×2) structure, in agreement with the experimental LEED observations.

Other non-structural experiments such as valence band and core-level photoemission experiments or early STM measurements have been interpreted in the framework of the DDRM [58–60]. However, the recent real-space atom-resolved STM measurements by tunnelling for the first time into the unoccupied electronic states (presented above) question both DDRM and SDRM [27]. Indeed, each spot observed in the occupied states splits in the unoccupied states into two spots of unequal intensities that can be assigned to individual

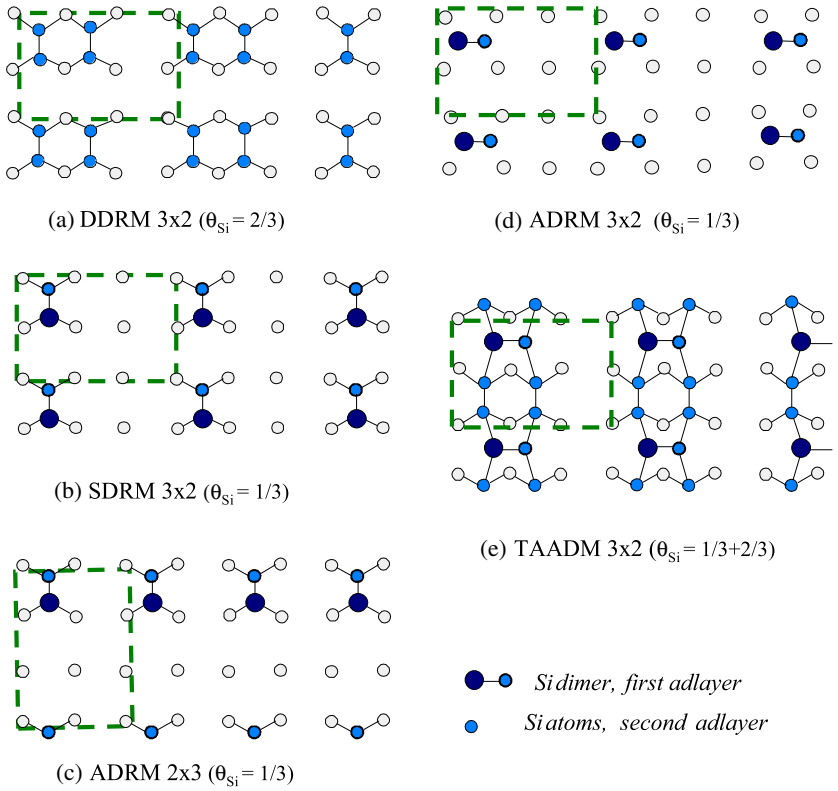

Figure 6. Schematic top views of the β-SiC(100) 3×2 surface reconstruction proposed models: (a) DDRM [26, 55, 56, 58–60], (b) SDRM [53, 54], (c) ADRM 2×3 [39, 61], (d) ADRM 3×2 [27] and TAADM [62, 63]. The corresponding primitive $3 \times 2/2 \times 3$ surface unit cells are indicated by a dashed line.

atoms. Therefore, the Si atoms forming the dimers are resolved in the unoccupied states, and unambiguously indicate that the dimers are perpendicular to the dimer rows along the $\times 2$ direction. On the grounds of this STM observation, a sketch is proposed for the last surface plane, with asymmetric dimers perpendicular to the dimer rows and a total $1/3$ ML coverage (figure 6) [50]. However, the STM technique is sensitive to the topmost atomic layer only, and cannot explain how these dimers, oriented along the $\times 3$ direction, can be connected to the underlying Si atomic plane in order to agree with the experimental observation of a $2 \times 1/c(4 \times 2)$ (and not a $1 \times 2/c(2 \times 4)$) reconstruction for the Si-terminated surface.

At this point, we mention that some models are also derived from *ab initio* theoretical calculations. First, an asymmetric dimer row model (ADRM) has been proposed involving two silicon atomic planes, with a $1/3$ ML coverage for the last plane [39, 61]. In this model, the last atomic plane structure agrees with the sketch derived from the previous STM observations [27]. But this structure exhibits a 2×3 periodicity in strong contradiction with other experimental evidence (figure 6). Recently, another model was proposed, the two adlayer asymmetric dimer row model (TAADM) involving three Si atomic planes instead of two [62, 63]. This TAADM model is the combination of the ADRM 3×2 [27] on top of the DDRM [55–57], where the first adlayer is identical to the ADRM 3×2 top $1/3$ ML atomic plane and lies on a second adlayer similar to the DDRM top $2/3$ ML atomic plane, instead of being directly connected to an Si-terminated surface.

The orientation of the topmost dimers has been studied through a 3×2 to a 3×1 phase transition that seems to take place upon room temperature atomic hydrogen exposure, as reported using LEED experiments [64]. Actually this transition has been assigned to Si–Si dimers breaking, which would imply that the dimers are parallel to the $\times 2$ periodicity [64]. However, real-space STM measurements in the unoccupied states before and after atomic hydrogen exposure with the surface kept at $T = 300\,^{\circ}\mathrm{C}$ show some reactive sites (see below) made of bright double spots of equal intensity, which correspond to reactive top-most dimers becoming symmetric [65]. According to this STM observation, the reactive top-most dimers are not broken. Furthermore, the general 3×2 surface ordering remains unchanged even if the surface is reactive [65]. Therefore, the reported 3×1 LEED structure [64] is not conclusive. One can rather interpret this observation by a defect-induced loss of $\times 2$ long-range periodicity. Actually, on clean surfaces, we have shown above that one observes the so-called 'dimer-pair defect' and the correlated one-half unit cell parameter shift along the dimer row [27]. This kind of defect leads to long anti-phase boundaries and is responsible for the long-range periodicity weakening along the $\times 2$ direction. Such an effect existing on the clean surface may indeed be enhanced by atomic hydrogen interaction. Notice also that such a 3×1 LEED pattern has been observed to result from oxygen contamination of the β-SiC(100) 3×2 surface [56].

In order to discriminate between these various models, some of the valence-band spectroscopy photoemission experiments [58–60] have been revisited in order to compare the experimental data to recent theoretical calculations [62]. The available data can find some agreement only with the surface bands calculated for the TAADM, whereas both DDRM and SDRM are ruled out. However, such a comparison cannot be conclusive since there are very few available experimental data, and especially no data along the dispersing J–M and M–J' directions. Also some reflectance anisotropy spectroscopy measurements have been performed [66] and experimental data compared to reflectance theoretical calculations [67], but in that case, it is really difficult to discriminate between TAADM and DDRM which both exhibit two similar broad spectral features [67].

A structural tool is therefore required to discriminate between these different models. For this purpose, we turn to grazing incidence x-ray diffraction (GIXRD) [50], which has been especially successful in solving accurately complex surface structures [68–70]. The GIXRD experiments using synchrotron radiation were performed on the CRG-IF (BM32) beam line (ESRF-Grenoble) at a 3×10^{-11} Torr pressure, keeping a very high surface quality during all the measurements. Because of the lack of high-quality cubic SiC single crystals, such an experiment was done on a single crystal thin film (1 μm). This latter was grown by CVD on a carbonized Si(100) wafer with a buffer layer at the SiC/Si interface having rather large stacking fault defect densities, making surface measurements especially challenging. In order to eliminate the contribution coming from the stacking faults, we used a low photon energy at 12 keV and an incidence angle below the critical angle value. As compared to a standard semiconductor study, the reciprocal space area probed was therefore reduced. In addition, a specific sample mounting was needed for homogeneous high-temperature annealings through direct current heating, further reducing the probed area. High-quality β-SiC(001) 3×2 single domain surfaces were checked by RHEED and GIXRD. The basis vectors (a_S, b_S, c_S) of the surface reconstruction unit cell are related to the bulk ones by $\mathbf{a}_S = [1\bar{1}0]_{\mathrm{bulk}}$, $\mathbf{b}_S = [110]_{\mathrm{bulk}}$, $\mathbf{c}_S = [001]_{\mathrm{bulk}}$, with $a_S = b_S = 3.088$ Å and $c_S = 4.367$ Å. The reciprocal space is described by its reduced coordinates (h, k, l), l being perpendicular to the surface. Two complete sets of data (measured from two distinct 3×2 surfaces) are in excellent agreement. For each set, we measured 78 inequivalent in-plane and 276 out-of plane reflections, along 8 inequivalent rods, and 168 reflections along 5 inequivalent crystal truncation rods (CTR) [68–70]. For the analysis, the diffracted intensities along the $\times 2$ direction, which are too weak, likely resulting

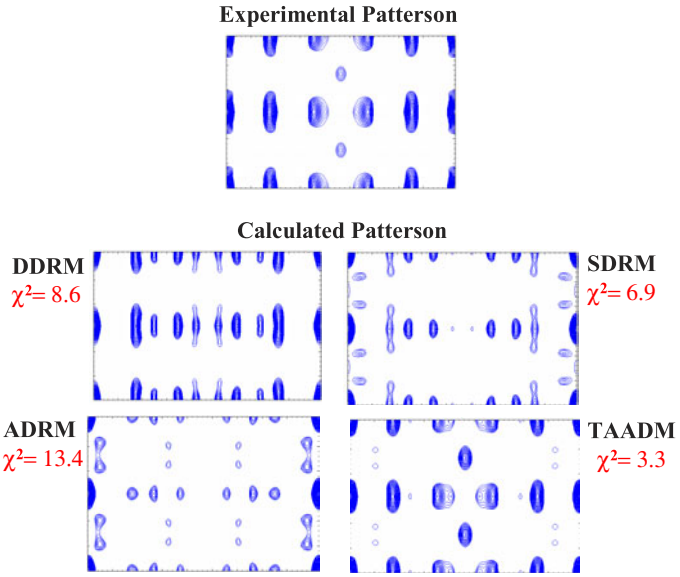

Figure 7. Experimental and calculated Patterson function maps for the different existing models of the β-SiC(100) 3×2 surface reconstruction. The experimental Patterson function is derived from the in-plane diffracted intensity of the β-SiC(001) 3×2 surface measured at $l = 0.05$. The calculated Patterson functions are derived from the fit of the first adlayer atomic positions assuming a $p2mm$ symmetry. The corresponding χ^2 agreement factors are also displayed for each model.

from Si dimer pair formation (defect B) as identified by atom-resolved STM, were not taken into account [27].

From the in-plane diffracted intensities, measured at $l = 0.05$, the experimental Patterson function was derived (see figure 7), and therefore the in-plane interatomic vectors in the unit cell could be determined [68–70]. The experimental Patterson function exhibits a $p2mm$ symmetry that is consistent with either a $p2mm$ (two perpendicular mirrors), $p1m$ (one mirror), or $pm1$ symmetry of the unit cell. First, the experimental diffracted intensities were compared with the calculated ones for each model, in the framework of a $p2mm$ symmetry. Therefore, a fit of the atomic positions of the first adlayer could be achieved for each model. The different models can be evaluated through the least-square residual agreement factor χ^2 that takes into account a 10% experimental error bar. As displayed in figure 6, all models yield χ^2 values much larger than the satisfactory value of 1 with 13.4 for the ADRM, 8.6 for the DDRM, 6.9 for the SDRM, the TAADM being the closest at $\chi^2 = 3.3$. For comparison, the corresponding calculated Patterson functions are shown in figure 7.

Therefore, the TAADM was chosen as a starting point, and the in-plane diffracted intensities were fitted by also relaxing the in-plane atomic positions of the underlying atomic planes. However, within the $p2mm$ symmetry, one could not achieve a χ^2 better than 2.5. Therefore, we reduced the symmetry conditions and performed the fit on the basis of a $p1m$ symmetry. The top dimer was therefore allowed to be asymmetric while the underlying dimers may have different lengths. Using this fitting procedure, the least mean square residual minimization led to a $\chi^2 = 1.4$ value for the reconstruction in-plane intensities. Thus, one could conclude that the $p1m$ symmetry is correct, and apply the fitting procedure to the whole data set, including both in-plane and out-of-plane reconstruction rods intensities, leading to a very satisfactory $\chi^2 = 1.2$ factor. This fitting agreement is illustrated in figure 8 by the

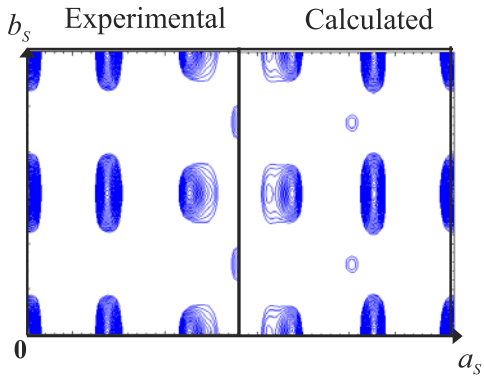

Figure 8. Experimental (right) and calculated (left) half Patterson contour plots for the ALSD model of the β-SiC(001) 3×2 surface reconstruction, represented over the whole 3×2 unit cell with a vertical plane in the centre of the unit cell. 50 contour levels are used between the 0.14 and 1 minimal and maximal values. The fitting procedure was performed for the in- and out-of-plane reconstruction rods data in the framework of a $p1m$ symmetry.

comparison between the experimental and the calculated Patterson functions. The diffracted intensities along the surface rods give some insights about the out-of-plane atomic positions. Four different representative profiles are shown in figure 8, along the $(5\bar{2}l)$, $(50l)$, $(10l)$ and $(80l)$ surface reconstruction rods. The fitting curve average modulation period is found between 2.5 and 2.8 in the reciprocal lattice coordinates, which corresponds to a 2.3 Å direct space thickness, indicating that the reconstruction involves more than two silicon atomic layers.

The fitting procedure allows us to determine the in-plane and out-of-plane coordinates of the 12 atoms involved per reconstruction unit cell. First, we notice that the silicon atomic planes are distant by $a_0/3$, a_0 being the unit lattice parameter, instead of $a_0/4$, the bulk interlayer distance, evidencing the open character of the surface. The dimers of the first adlayer are found to be asymmetric, in agreement with the STM measurements [27], but the results indicate a 0.1 Å height difference, much less than the calculated height at 0.5 Å in the TAADM [62]. The most striking feature is that the underlying dimers of the second adlayer have different lengths, namely a long one at 2.41 Å and a short one at 2.26 Å, in contrast with the TAADM where both dimers were calculated to have the same length at 2.37 Å, somewhat closer to the long dimer. The alternating long (D_{L}) and short (D_{S}) dimers are bonded on both sides respectively to the up (A_{U}) and down (A_{D}) atoms of the top asymmetric dimers.

The CTR could be fitted with a $\chi^2 = 2.5$ indicating a rather flat surface with a negligible roughness ($\beta = 0.08$). Two representative profiles are shown in figure 9 for the $(60l)$ and the $(30l)$ CTR. From the (300) anti-Bragg reflection, one can deduce a 300 Å average terrace length, in agreement with STM measurements [27]. According to the CTR fit, the surface reconstruction is registered to the bulk with slight deviations ($\Delta x = 0.03$ Å, $\Delta z = 0.03$ Å) of the deeper third silicon atomic plane atoms from bulk positions.

The alternative long and short dimers (ALSD) model derived from the grazing incidence x-ray diffraction data analysis is shown in figure 10. The structure is in agreement with the theoretical TAADM for the surface morphology, involving three Si atomic planes with respectively 1/3 ML and 2/3 ML for the first and second adlayers that are lying on a third full atomic silicon plane. However, the second silicon adlayer presents a long-range organization with alternating long and short dimers (ALSD) that was not predicted in the *ab initio* calculations [62]. Surface stress minimization is already known to be responsible for the Si-terminated alternatively up and down dimers (AUDD) surface structure [28]. In the 3×2

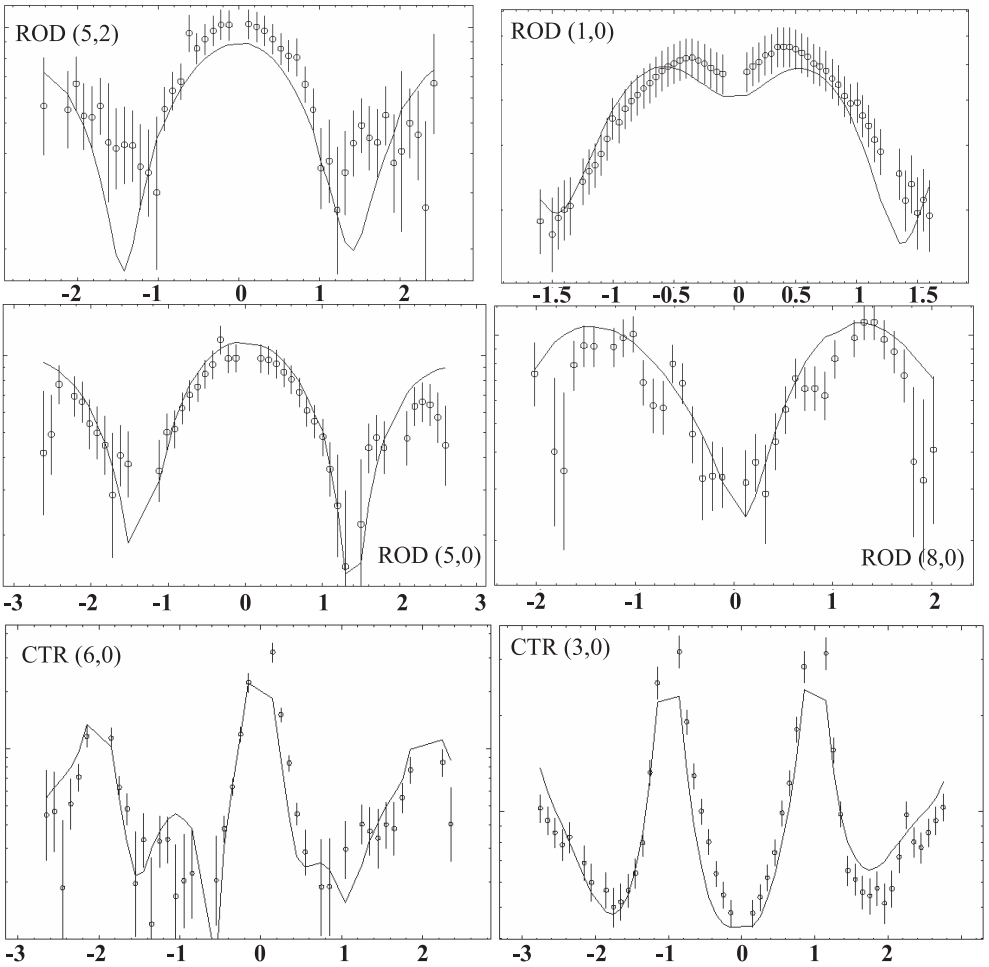

Figure 9. $(5\bar{2}l)$, $(10l)$, $(50l)$ and $(80l)$ surface reconstruction rods and $(60l)$ and $(30l)$ crystal truncation rod (CTR) profiles with the error bars and corresponding fits. The logarithm of the absolute value of the structure factor is represented as a function of the out-of-plane reciprocal lattice coordinate l.

structure, this silicon atomic plane becomes the third deeper one, and in this configuration lies very close to the bulk atomic positions. One can therefore imagine that the stress has been 'transferred' to the next silicon plane. In this view, the second adlayer is expected to minimize the surface stress and to encounter a kind of AUDD reconstruction. Actually, the stress minimization occurs in a slightly different way, probably because a 1/3 ML Si plane lies above, leading an ALSD structure to develop instead of an AUDD one. Furthermore, this long-range organization of the second adlayer can explain why all the dimers of the first adlayer are tilted in the same direction.

Another very interesting aspect of the above ALSD model is that it shows a very open β-SiC(100) 3×2 surface reconstruction having a large distance between the first and second and between the second and third Si atomic planes at 1.56 Å, significantly larger than the interatomic layer spacing in bulk SiC and bulk Si with values at 1.09 and 1.35 Å respectively. Furthermore, a 3.43 Å distance between non-dimerized Si atoms within the same third plane

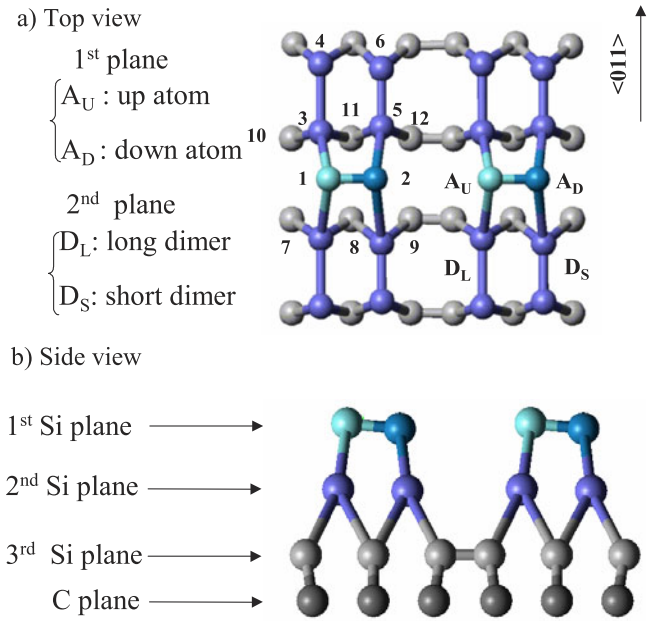

Figure 10. (a) Top and (b) side views of the β-SiC(001) 3 × 2 surface reconstruction showing the three Si atomic planes with the top A_U–A_D asymmetric dimers (first plane) and the ALSD dimers having alternating long D_L and short D_S lengths in the second plane.

is also significantly larger than the bulk value of 3.08 Å. One can correlate this finding to the rather high reactivity of the Si-rich β-SiC(100) 3 × 2 surface with simple adsorbates such as hydrogen or oxygen when compared to silicon, with H(O) atom insertion into the subsurface region already taking place at very low exposures [65, 71, 72]. This indicates that this very open surface facilitates hydrogen or oxygen atom insertion into the β-SiC(001) lattice, which is of both strong fundamental interest and technological importance.

3.3. The Si-terminated β-SiC(100) c(4 × 2) surface reconstruction

3.3.1. The atomic structure of the c(4 × 2) reconstruction determined by atom-resolved STM and STM image simulations. Due to the expected analogy with the structure of corresponding Si(100) and Ge(100) surfaces [22, 23], the β-SiC(100) 2 × 1 and β-SiC(100) c(4 × 2) surface reconstructions are of special interest. In fact, it was initially believed that the β-SiC(100) 2 × 1 surface reconstruction was the ground state since a 2 × 1 LEED pattern was observed for the stoichiometric Si-terminated surface [26]. The c(4 × 2) LEED patterns were also observed for Si-terminated surfaces showing the existence of such a reconstruction [26, 73, 74] and suggesting a surface structure similar to that of Si(100) c(4 × 2) and Ge(100) c(4 × 2) with anticorrelated asymmetric Si–Si (Ge–Ge) dimers [22, 23]. However, in contrast to these elemental covalent semiconductors which exhibit such a reconstruction at low temperatures only, the c(4 × 2) array takes place at room temperature for the β-SiC(100) surface as for the 2 × 1 surface reconstruction for the Si and Ge [74]. In fact, it was shown that the Si(100) c(4 × 2) exhibits 2 × 1 LEED patterns and STM topographs when slightly contaminated or in the presence of high defect densities [75]. Also, one has to keep in mind that the stoichiometric β-SiC(100) surface is a stressed surface when compared to other semiconductors. In fact, due to the large difference between the lattice parameters, the

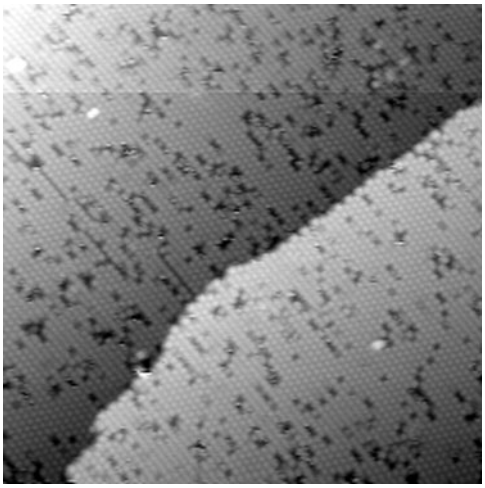

Figure 11. A β-SiC(100) c(4×2) surface: 400 Å×400 Å STM topograph (filled electronic states). The sample bias was $V_s = -3$ V with a 0.2 nA tunnelling current.

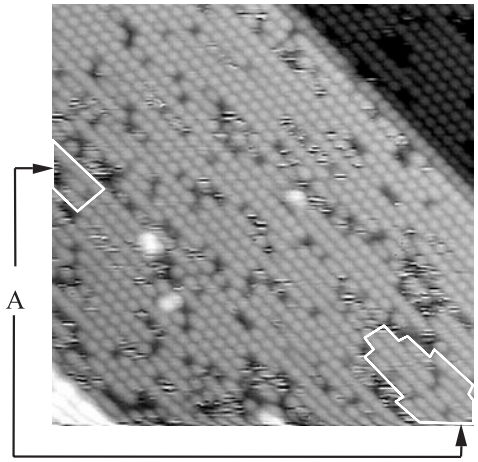

Figure 12. (a) A β-SiC(100) c(4 × 2) surface 200 Å × 200 Å STM topograph (filled electronic states). Examples of an area having lower corrugations in a 2 × 1 array are labelled A. The sample bias was $V_s = -3$ V with a 0.2 nA tunnelling current. (b) Details of an area showing the pseudo-hexagonal dimer array and the c(4 × 2) unit cell.

Si atoms on an Si-terminated β-SiC(100) surface are 'compressed' by ≈20% when compared to the situation of Si(100) 2 × 1. This key factor is likely to have major consequences and to result in a very specific surface structure. Also, contrary to the 3 × 2 surface reconstruction which is a very open surface with a 1/3 + 2/3 + 1 Si ML coverage [50], the c(4 × 2) surface is completed at a full 1 ML Si coverage [8, 26, 53].

In order to clarify these points, atom-resolved scanning tunnelling microscopy experiments were performed [28]. Figure 11 shows a representative 400 Å × 400 Å STM topograph (filled electronic states). The pattern exhibits a characteristic pseudo-hexagonal array in which each spot represents an Si–Si dimer as confirmed by STM image calculations using the STM elastic-scattering quantum chemistry (STM-ESQC) method, with the bulk substrate and the tip body both modelled by a four-layer semi-infinite repetition of an SiC(100) unit cell [28]. While this surface seems to present a somewhat higher defect density, it shows only very few antiphase boundaries (three of them can be seen for example in figure 10) having a length limited to $\leqslant$50 Å which significantly differs from the behaviour of the 3 × 2 surface—see above [27]. Figure 12 provides a closer look at this surface: in some areas having higher defect densities, one can see that the corrugation deteriorates with an ordering corresponding to a 2 × 1 domain in areas marked A [28], in agreement with previous LEED reports [31]. When making dimer height plots along the XX' (perpendicular to dimer rows) and YY' (along the dimer rows) axes, one can clearly see the existence of additional density of states between two dimers belonging to the same row (figure 13). The experimental plots are found to be in excellent agreement with STM-ESQC calculations performed with constant current height profiles along the XX' and YY' axes (figure 13(b)) for various up-dimer down-dimer height differences at $\Theta = 1$ ML (also at $\Theta = 1/2$ ML for missing down-dimers). Comparison with experimental scans shows that the best agreement for both the XX' axis and the YY' axis is reached for a height difference of $\partial z = 0.1$ Å (figures 13(a) and (b)). This interesting feature suggests the existence of an additional Si–Si dimer which would be located below the surface between two

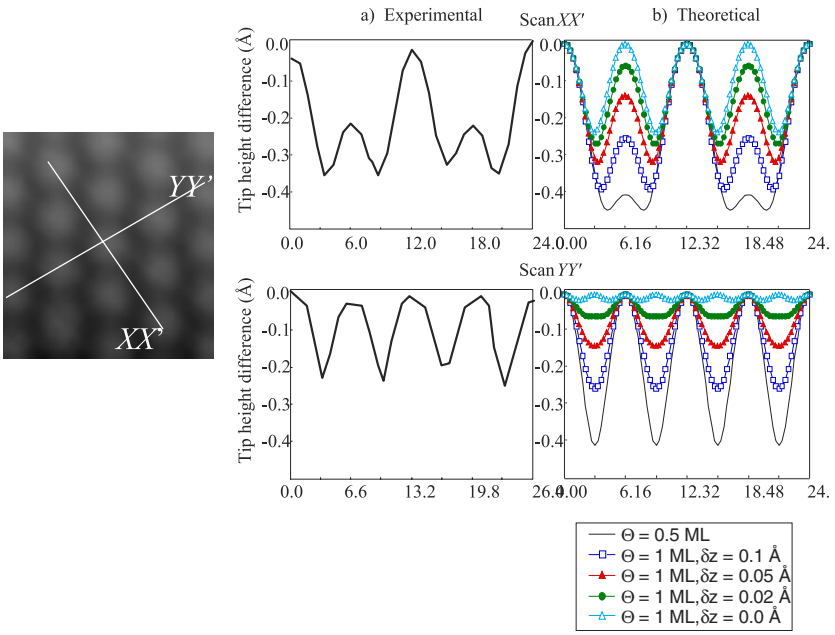

Figure 13. A β-SiC(100) c(4 × 2) surface: (a) STM experimental height profiles along the XX' axis (top) showing two components corresponding to up- and down-dimers, and the YY' axis (bottom) showing the component corresponding to up-dimers. (b) Theoretical height profiles for various up-/down-dimer height differences along the XX' (top) and YY' (bottom) axes calculated in a constant current mode ($I = 0.2$ nA) at the top of the β-SiC(100) valence band.

dimers 'visible' to the STM tip [28]. Such a picture of dimer rows having up- and down-dimers (AUDD) within a row is therefore strongly supported by the theoretical ESQC-STM height plot. These calculations also indicate that, when the height difference ∂z between the up- and the down-dimer is above 0.1 Å, the down-dimer would remain hidden to the STM tip [28].

These STM results indicate that this array of dimer rows having up- and down-dimers (AUDD) within a row leads to an arrangement reducing the very large surface stress occurring on the c(4 × 2) surface reconstruction. A model of this reconstruction is provided in figure 14, which also displays the corresponding experimental STM topographs and calculated images [28]. Incidentally, one should notice the excellent agreement between the STM topograph and the calculated image [28]. Such an AUDD surface structural model has never been observed for any other surface reconstructions. Furthermore, the structure of the β-SiC(100) c(4 × 2) reconstruction (AUDD) is very different from that of corresponding elemental semiconductors such as Si(100) c(4 × 2) and Ge(100) c(4 × 2) [45, 46]. In fact, contrary to the case of covalent semiconductor surfaces in which dangling bond reduction is at the origin of surface reconstructions, surface stress reduction seems to be the leading driving force in this AUDD surface arrangement, resulting in a c(4 × 2) array [28]. This also explains why 2 × 1 surface domains are found in an area having higher defect densities [28]. In this case, defects and/or vacancies would locally release the surface stress, allowing the up- and down-dimers to have the same height [28]. This explains why the 2 × 1 surface was initially found in pioneering works to be the ground state of the stoichiometric Si-terminated β-SiC(100) surface reconstruction [28]. Actually, the 2 × 1 surface observed at room temperature results from a failed c(4 × 2) surface reconstruction.

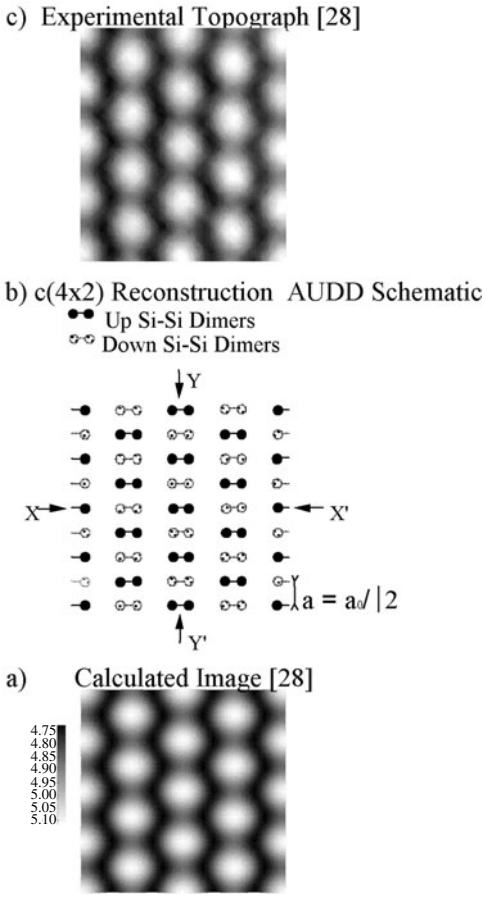

Figure 14. A β-SiC(100) c(4 × 2) surface reconstruction. (a) Calculated STM image (the same conditions as in figure 3(b)) for a coverage $\Theta = 1$ ML and up- and down-dimers separated by 0.1 Å. The corrugation is 0.27 Å from black to white. (b) Schematic diagram of the β-SiC(100) c(4 × 2) surface showing the alternating up- and down-dimers (AUDD). The non-reconstructed surface primitive lattice parameter is $a = a_0/\sqrt{2}$, where $a_0 = 4.36$ Å is the β-SiC lattice constant. (c) An experimental STM topograph. For the sake of comparison with the calculated STM image (figure 14(a)), the contrast has been enhanced and the picture rotated by 42°.

So far, only the up-dimer of the β-SiC(100) c(4 × 2) surface reconstruction has been identified by STM probing only the filled electronic states [28]. We now probe the same surface using a dual scan mode, allowing us to probe both filled and empty electronic state topographs of the same area of the surface. Figures 15(a) and (b) respectively display the STM topographs of filled and empty states of the c(4 × 2) surface reconstruction [76]. Interestingly, both of them exhibit a similar pseudo-hexagonal pattern of spots representing Si–Si dimers, with each spot of the filled state image representing the up-dimer while the empty states topograph shows down-dimers [76]. In figure 15(b), one can see that the up-dimers (marked by circles) come between the down-dimers, as indeed expected for the AUDD model [28]. Most interestingly, the STM results also show that both dimers have very different electronic status, with the down-dimer partially filled and partially empty while the up-dimer is almost totally filled [76]. So, these STM measurements tunnelling into the empty electronic states further support the β-SiC(100) c(4 × 2) surface reconstruction results from Si–Si dimer rows

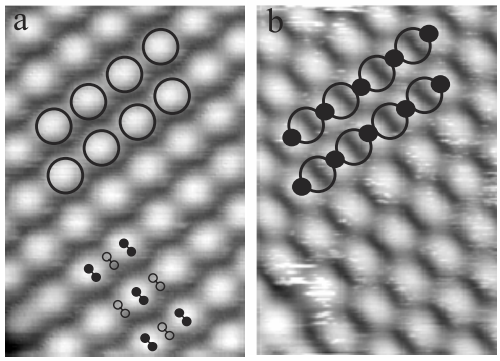

Filled Electronic States *Empty Electronic States*

Experimental STM topographs [76]

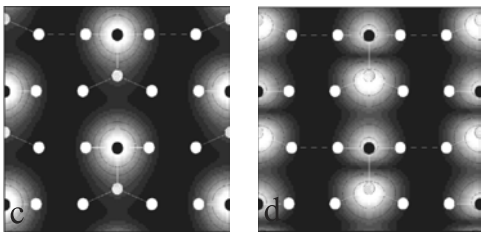

Filled Electronic States *Empty Electronic States*

Calculated STM images for the MRAD model [62])

Figure 15. A β-SiC(100) c(4 × 2) surface reconstruction. Top: a 48 Å × 33 Å STM topograph of (a) filled and (b) empty electronic states of using a dual scan mode. The tip bias was $V_t = +3$ and -3 V at 0.2 nA tunnelling currents. As a guide for the eyes, the circles indicate maxima of filled states and dark points show maxima of empty states. Up- and down-dimers are schematically represented in (a). Bottom: calculated STM images for the MRAD model after [62].

having alternating up- and down-dimers (AUDD model) within the row [28, 76]. Notice that the c(4 × 2) surface reconstruction is highly sensitive to background contamination with a short surface lifetime becoming 2 × 1 in poor vacuum conditions, most likely resulting from the high surface sensitivity to molecular hydrogen [77]. Finally, one should remark that this very particular AUDD surface ordering has not been observed before for any other surface, and results from a large surface stress as already indicated above [28].

3.3.2. Ab initio total energy calculation studies of the c(4 × 2) *reconstruction.* The AUDD model is further supported by *ab initio* total energy calculations [43, 44]. *Ab initio* total energy DMol^{TM} cluster calculations were performed using density functional theory (DFT) with local density approximation (LDA) to study this reconstruction. This rather simple calculation, performed on a cluster having 137 atoms, exhibits spontaneous AUDD formation [44]. In addition, it indicates that the Si–Si dimers also have alternating lengths with the up-dimer being longer (2.50 Å) than the down-dimer (2.27 Å) with a 0.23 Å height difference between them [44]. Figure 16 provides the model cluster used for this calculation, and shows an AUDD dimer row better. State-of-the-art molecular dynamics total energy calculations using DFT-LDA with a slab model also find AUDD ordering of the c(4 × 2) surface when a stress is indeed applied to the slab, indicating further its possible role in the surface organization [43].

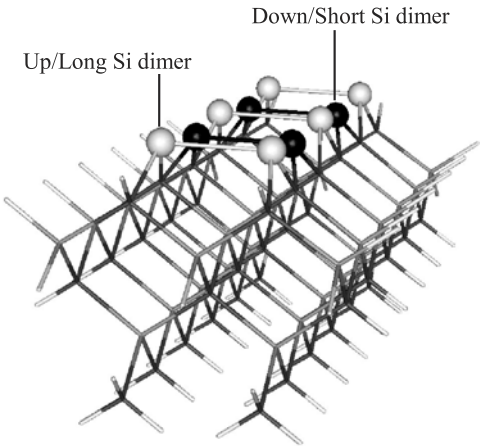

Figure 16. The 3D Cluster of 137 atoms used in the DMol calculations of the β-SiC(100) c(4 × 2) surface reconstruction showing at the topmost surface the Si–Si dimers having alternating heights (up and down) and lengths (long and short).

Another calculation recently proposed an alternative model for the β-SiC(100) c(4 × 2) surface reconstruction, the so-called missing asymmetric dimer row (MRAD) model [45, 63]. The latter, which is primarily based on the calculation of the Si formation energy versus the Si chemical potential, has a very different morphology and structure, with a surface reconstruction including two Si atomic layers having coverages of 0.5 + 1 ML on top of the first C atomic plane [45, 63]. However, one should mention that the MRAD model has so far received no support from any experimental investigation. The 0.5 Si ML coverage description of the topmost atomic surface layer of the c(4 × 2) reconstruction [45] is inconsistent with the various experimental evidence of a surface terminated by a 1 Si ML atomic layer [35, 53]. We will see below that the MRAD model cannot satisfactory explain the temperature-induced c(4 × 2) − 2 × 1 metallic phase transition [35, 75]. In addition, one should also notice in figure 14 that the experimental topographs for the empty electronic states (figures 15(a) and (b) respectively) are inconsistent with the STM image simulations (filled and empty states in figures 15(c) and (d) respectively) calculated for the MRAD model [45], stressing again that the MRAD model is not suitable for describing the c(4 × 2) surface reconstruction [76]. Overall, this indicates that silicon carbide seems to remain a challenge for LDF approaches [35] despite the fact that these *ab initio* calculations have been especially useful for the understanding of the structure and properties of surfaces, including those of semiconductors.

3.3.3. Synchrotron radiation-based core level photoemission at the β-SiC(100) c(4 × 2) surface In order to obtain deeper insights about the c(4 × 2) surface reconstruction, high-resolution core level photoemission spectroscopy using synchrotron radiation at the Si 2p core level were performed at various photon energies using the energy tunability of the synchrotron light source. In this way, it was possible to probe fine structural details of both surface and subsurface regions and to get insights about the stress influence below the surface. Figure 17 displays a representative set of Si 2p core level spectra at various photon energies from bulk to surface sensitive ones [49]. The Si 2p core level decomposition was performed in the entire photon energy range (115–130 eV) using a 85 meV Lorentzian width, a 602 meV spin–orbit splitting and a 600 meV Gaussian width, the latter being three times larger than for bulk Si 2p for silicon [49].

Using the photoelectron mean free path versus photon energy and peak decomposition (figure 17) the Si 2p is shown to have several components including: (i) two Si 2p surface shifted components S1 and S2, (ii) two subsurface shifted components SB1 and SB2, and (iii) one

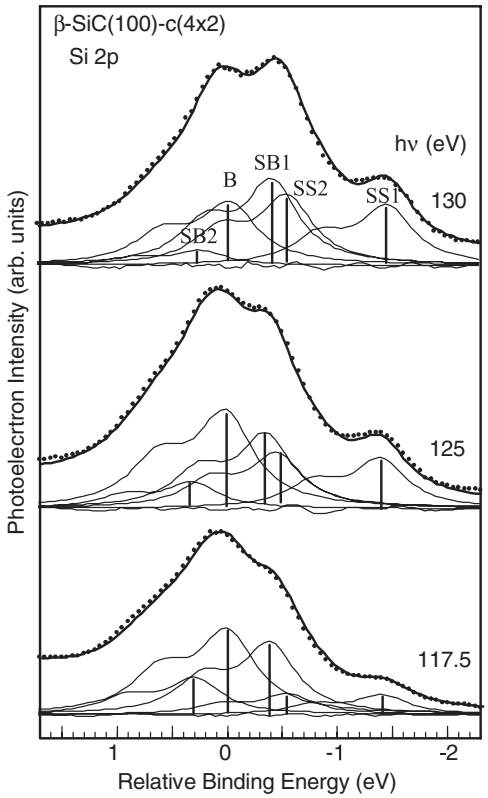

Figure 17. A β-SiC(100) c(4×2) surface reconstruction. Representative decompositions of three of the Si 2p photoelectron spectra for photon energy ranging from 117.5 eV (bulk sensitive mode) to 130 eV (surface sensitive mode). Parameters used for the decompositions: spin–orbit splitting of doublets -0.602 eV; branching ratios -0.5 eV; Lorentzian -0.085 eV; Gaussian -0.6 eV (bulk component) and 0.55 eV (all other components). The results and residues of fits presented by solid curves overlapped with experimental points and at the bottom of each spectrum correspondingly. The Si $2p_{3/2}$ energy positions of the four shifted components relative to B are +0.3 (SB1), -0.5 (SB2), -0.9 (S2), and -1.4 eV (S1) as a average from the fitting of the 10 different spectra. Integrating the background was used in the fitting procedure of all spectra except for the spectrum recorded at a photon energy of 115 eV, where an exponential one was used.

bulk component B (figure 17). The S1 and S2 surface core level shifted components are respectively related to the up- and down-dimers [49]. Interestingly, S1 (up-dimer) has a much lower binding energy (-0.8 eV) than S2 (down-dimer), indicating a very significant difference in their electronic status, the down-dimer being much emptier than the up-dimer [49]. This behaviour is actually in excellent agreement with the filled and empty electronic states STM topographs that are described above. Notice that the intensity of the Si 2p surface core level shift (responsible for SS1) decreases as soon as the c(4×2) surface become defective and/or contaminated, stressing that this spectral feature does not result from defects as previously believed. The sharpness and high intensity of the spectral feature (located at -1.4 eV, figure 17) responsible for SS1 is a clear indication of a high-quality β-SiC(100) c(4×2) surface.

Significant insights about the subsurface region could be found by looking at the behaviour of SB1 and SB2 components. Of principal interest is the intensity dependence versus photon energy of SB1 and SB2, which significantly differ from each other, as can be seen from figure 18: SB1 and the bulk component exhibit a very similar behaviour at bulk-sensitive

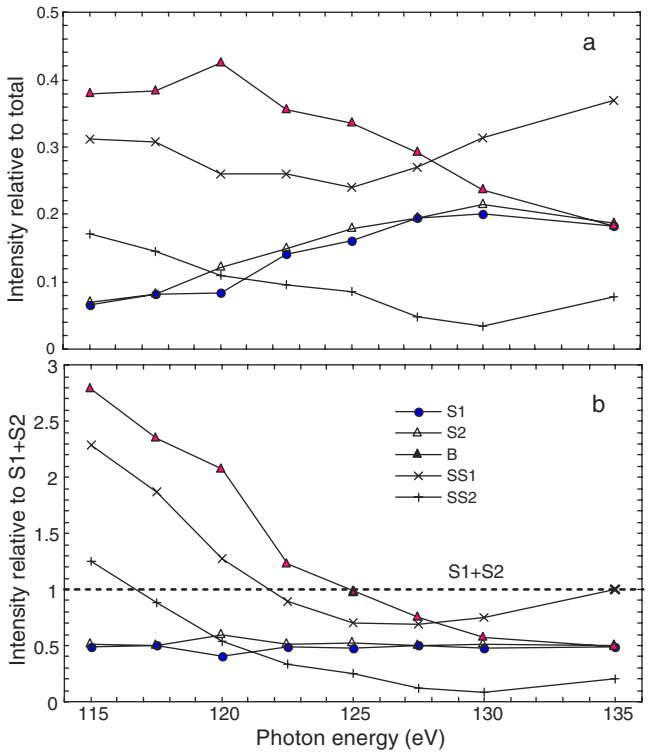

Figure 18. (a) The fraction of total intensity for the Si 2p decomposed components obtained from fits of c(4 × 2) spectra with different photon energies. (b) The same as in (a) but normalized to the top surface layer, presented by $S_1 + S_2$ intensities. The lines are drawn as a guide for the eyes.

photon energies (115–125 eV) indicating a more dominant bulk contribution for SB1 [49]. Instead, SB2 is more 'surface sensitive-like', showing that SB2 is related to subsurface atoms located in the layers below the surface [37]. The behaviour of SB1 indicates that, well below the surface, Si atoms are still away from their 'bulk' position, suggesting that the subsurface (as the top surface layer) region is also significantly affected by stress deep into the bulk [49]. This finding is especially relevant for theoretical investigations in which the surface is represented by slabs with the bulk atom located at only a few atomic layers below the surface [49]. This might explain the origin of some of the discrepancies between theory and experiments. With the identification of the surface core level shifted components that are correlated to the up- and down-dimers, the present Si 2p core level photoemission spectroscopy results also favour the AUDD model [28, 43, 44, 74] of the Si-terminated β-SiC(100) c(4 × 2) surface reconstruction. However, these data are not consistent with the MRAD model [45].

3.4. The C-terminated β-SiC(100) c(2 × 2) surface reconstruction investigated by atom-resolved STM

As mentioned above in the introduction, the C plane of β-SiC(100) is 'stretched' by 22% when compared to C(100). So the C-terminated surface of β-SiC(100) is of special interest. The β-SiC(100) c(2 × 2) surface structure has been known for nearly a decade from low-energy electron diffraction (LEED) [30] and near edge absorption fine structure (NEXAFS) [31], and very recently has been revisited by photoelectron spectroscopy and diffraction techniques using synchrotron radiation [37]. The β-SiC(100) c(2 × 2) surface includes 'acetylene-like'

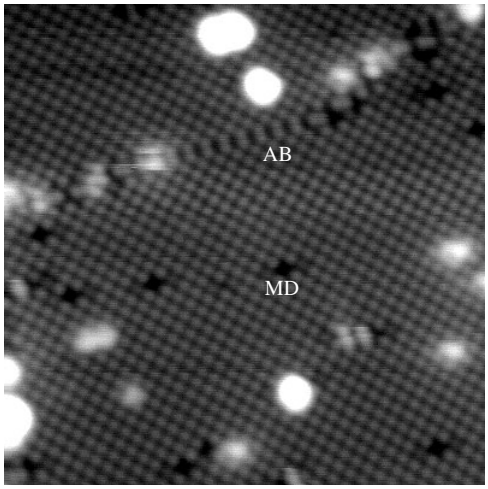

Figure 19. A C-terminated β-SiC(100) c(2 × 2) surface reconstruction. 150 Å × 150 Å STM topograph (filled electronic states). The tip bias was $V_t = +3$ V at a 0.2 nA tunnelling current. The two different types of defect mentioned in the text are marked MD and AB.

C≡C triple bond dimer (carbyne) rows in an sp configuration [30, 31, 37]. In addition, the C-terminated β-SiC(100) c(2 × 2) has been shown to behave very differently from Si-terminated surfaces upon adsorbate deposition: (i) upon donor adsorbate deposition such as alkali metals, the β-SiC(100) c(2 × 2) surface become metallic while Si-terminated surfaces remain semiconducting [78, 79]; (ii) the Si-rich and Si-terminated β-SiC(100) surfaces are very reactive to acceptor adsorbates such as oxygen, in contrast to the C-terminated surfaces which remain rather inert [80–82]. The C-terminated β-SiC(100) surfaces have also been investigated in detail by *ab initio* total energy calculations [39–42]. Very recently, the atomic scale fine details of the β-SiC(100) c(2 × 2) surface have been investigated using a real space probe such as scanning tunnelling microscopy, with a special emphasis on dimer tilt angle, defects and antiphase boundaries [34].

Figure 19 displays a representative 150 Å × 150 Å STM topograph (filled electronic states) of the β-SiC(100) c(2 × 2) surface reconstruction. It includes spots resulting from C dimers forming a c(2 × 2) surface arrangement in agreement with LEED photographs [30]. Also, two types of defects can be seen, including missing spots indicating a missing dimer (labelled MD) and double spot lines resulting from an antiphase boundary (labelled AB).

Figures 20(a) and (b) show 40 Å × 40 Å STM topographs (filled and empty electronic states respectively) of the β-SiC(100) c(2 × 2) surface with the corresponding plots along the C≡C triple bond dimer rows also represented [34]. Figure 20(a) shows the C≡C triple bond dimers forming the expected c(2 × 2) surface array. Looking at the empty electronic state topograph in figure 20(b), one can see that the spot observed in figure 20(a) splits into two different spots having different intensities. This behaviour is further evidenced when looking at the intensity plots along XX', showing one feature in figure 20(a) while two features (a), (b) can be seen in figure 20(b). This indicates that the C≡C triple bond dimers are asymmetric. The asymmetric nature of the C≡C triple bond dimers suggests that the surface stress is anisotropic, and probably extensive perpendicular to XX', i.e. to the dimer rows, and compressive along the dimer rows [34].

In addition to antiphase boundaries, the STM experiments show the interesting behaviour of the other type of defect for the c(2 × 2) surface, a missing dimer [34]. Figures 21(a) and (b) show such a defect as seen in STM topographs when tunnelling into the filled and empty states respectively. Of principal interest are the two bright spots observed near the missing dimer along XX' (i.e. along the C≡C triple bond dimer rows) in figure 21(b) (empty electronic states)

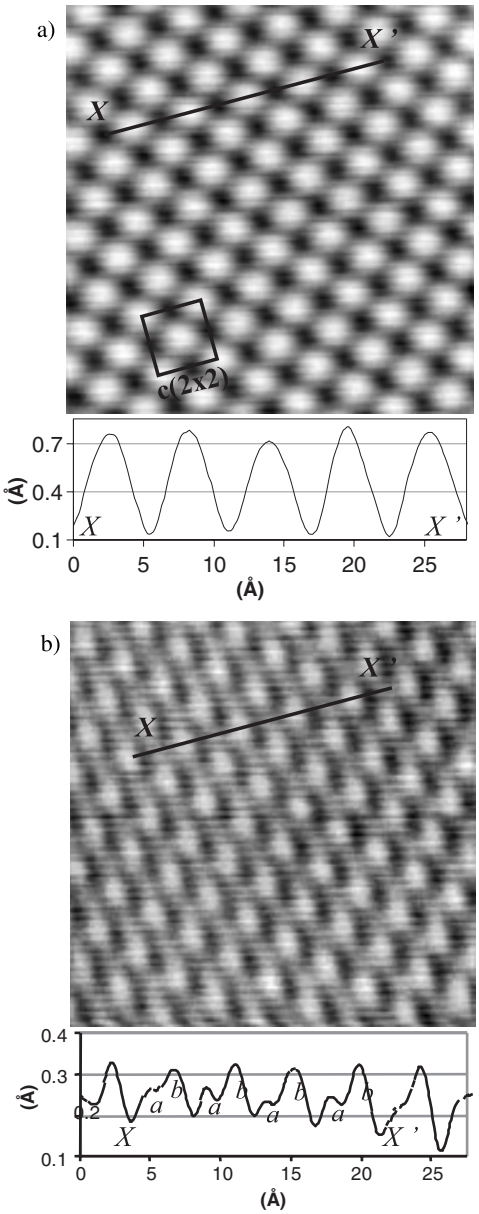

Figure 20. 40 Å × 40 Å STM topographs of the β-SiC(100) c(2 × 2) surface obtained by tunnelling into the filled electronic (a) and empty electronic states (b). Two height profiles along XX' are also displayed. The tip bias was $V_t = 3$ V (a) and -3 V (b) at a 0.2 nA tunnelling current.

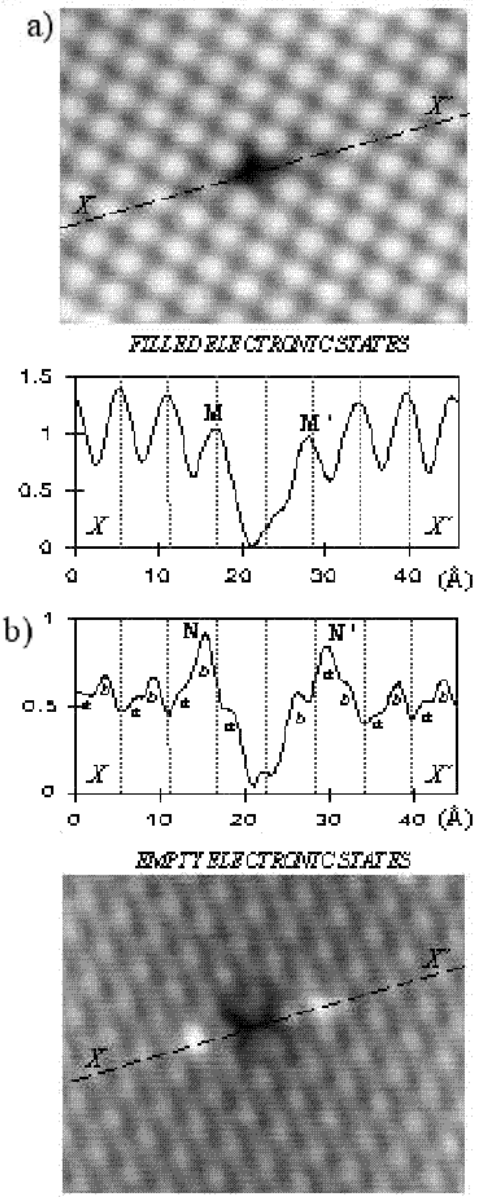

Figure 21. 40 Å × 30 Å STM topographs of a defect resulting from a missing dimer (MD) obtained by tunnelling into the filled electronic states (a) and empty electronic states (b). Two height profiles along XX' are also displayed. The tip bias was $V_t = +3$ V (a) and -3 V (b) at a 0.2 nA tunnelling current.

and not in figure 21(a) (filled electronic states) [34]. A better view of this situation can be seen in the corresponding intensity plots along XX' that are displayed in figures 21(a) and (b), M and M' corresponding to the dimer neighbours of the missing dimer, and N and N' their

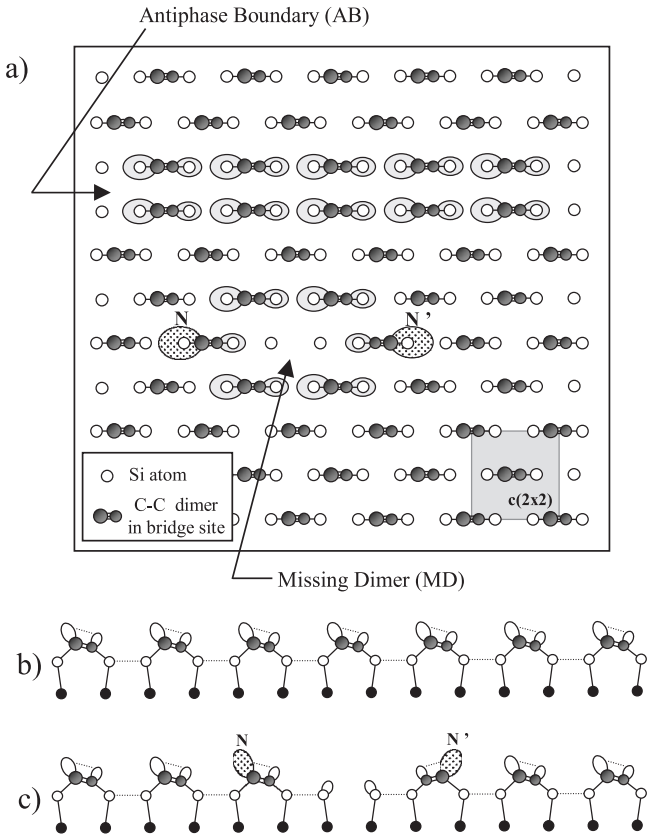

Figure 22. A schematic diagram of the β-SiC(100) c(2 × 2) surface structure. (a) Top view showing the unit cell of the c(2 × 2) reconstruction, a missing dimer and an antiphase boundary. Some of the dangling bonds have been represented around the two representative defects. (b) Side view along a dimer row and (c) side view along a dimer row including a missing dimer. N and N' indicate an excess of empty density of states of dangling bonds located near a missing dimer defect.

corresponding empty orbitals. This indicates an excess of empty density of states on the side of the missing dimer resulting from a charge transfer redistribution, which in turn tilts in the opposite direction the dimer located on the right of the missing dimer.

A model of the c(2 × 2) surface reconstruction is provided in figure 22(a), which displays a schematic top view of the surface general arrangement with tilted C≡C triple bond dimer rows, an antiphase boundary (AB) and a missing dimer (MD). Figures 21(b) and (c) respectively exhibit a side schematic view of a titled C≡C triple bond dimer row and the same with an MD defect showing the nearby dimers having opposite tilt angles and corresponding N and N' orbitals having an excess of empty electronic states [34]. This investigation shows very interesting and novel features and fine details about this particular C-terminated β-SiC(100) c(2 × 2) surface reconstruction [34].

4. The temperature-induced semiconducting c(4 × 2) ⇔ metallic 2 × 1 reversible phase transition

We now look at the effect of temperature on the c(4×2) reconstruction and on the resulting phase transition using high-temperature scanning tunnelling microscopy (HT-STM). Figure 23(a)

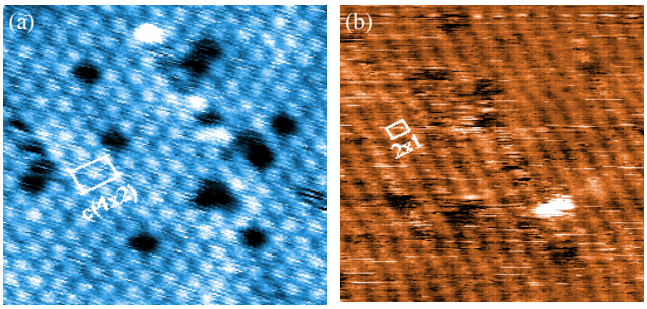

Figure 23. 100 Å × 100 Å STM topographs (filled electronic states). (a) β-SiC(100) c(4 × 2) at 25 °C; (b) β-SiC(100) 2 × 1 at 400 °C. The tip bias was +3.2 eV at a 0.12 nA tunnelling current.

displays a representative room temperature (RT) 100 Å × 100 Å STM topograph (filled electronic states) of a c(4 × 2) surface reconstruction having the characteristic pseudo-hexagonal pattern with each spot belonging to an Si–Si dimer [38]. As mentioned above, this structure results from dimer rows having alternately up- and down-dimers (AUDD) within the row, which reduces the large surface stress [28, 43, 44]. One can anticipate that the c(4 × 2) atomic arrangement would be significantly affected when the surface temperature is increased. We therefore performed high-temperatures STM imaging of the surface structure by maintaining the sample at 400 °C. Figure 23(b) shows a 100 Å × 100 Å STM topograph corresponding to this surface. The latter exhibits dimer rows that are characteristic of a 2 × 1 arrangement, which is further confirmed by the LEED photograph indicating a 2 × 1 surface array with a long range order [38]. Interestingly, when the surface is back at RT, both STM topographs and LEED photographs again exhibit a c(4 × 2) reconstruction, indicating that this phase transition is reversible [38].

Scanning tunnelling spectroscopy (STS) is a very powerful tool to probe local electronic surface properties, in order to get additional insights about this interesting c(4 × 2) $\Leftrightarrow$ 2 × 1 reversible phase transition. I–V measurements at RT and high temperature were performed for both c(4 × 2) and 2 × 1 structures and the results are shown in figure 24. Such curves are an average of 1000 I–V characteristics recorded over the 100 Å × 100 Å surface in equal steps [38]. The c(4 × 2) I–V curve (a) recorded at RT exhibits a horizontal section, clearly indicating its semiconducting nature. In contrast, the 2 × 1 I–V curve (b) recorded at 400 °C is almost linear and does not have any measurable gap. This very interesting behaviour demonstrates that the temperature-induced 2 × 1 surface reconstruction has a metallic character [38]. This metallization is evidenced by the first high-temperature STS measurements [38]. This c(4 × 2) $\Leftrightarrow$ 2 × 1 reversible phase transition could also be traced by looking at the electronic properties using valence band photoemission spectroscopy [83]. As can be seen in figure 25, the surface gap observed in the photoemission experiment closes at 400 °C when the surface undergoes a 2 × 1 ordering. At the same temperature, an electronic surface state characteristic of the c(4 × 2) surface reconstruction is destroyed while a finite density of states builds up at the Fermi level [83]. However, one notices that the density of states exhibits a monotonic power-law shape crossing the Fermi level [83], instead of a Fermi step expected for a normal metal. This change in the electronic density of states may be related to vibrational effects. Increasing the temperature leads to up- and down-dimers (AUDD) appearing, on average, at the same height, which gives the 2 × 1 surface arrangement observed at 400 °C. In this case, the distance between Si dimers belonging to the same row would be decreased to its minimum value at 3.08 Å which would in turn favour a significant overlap

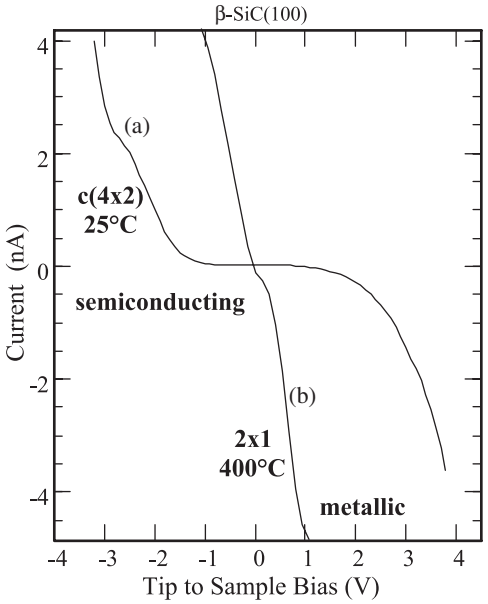

Figure 24. Tunnelling current versus voltage STS (I–V) for: (a) β-SiC(100) c(4 × 2) at 25 °C and (b) β-SiC(100) 2 × 1 at 400 °C. Each curve represents an average of 1000 I–V characteristics recorded on a grid in equal steps all over the 100 Å × 100 Å surface. Both curves were recorded using the same tip to sample distance. The sample was grounded.

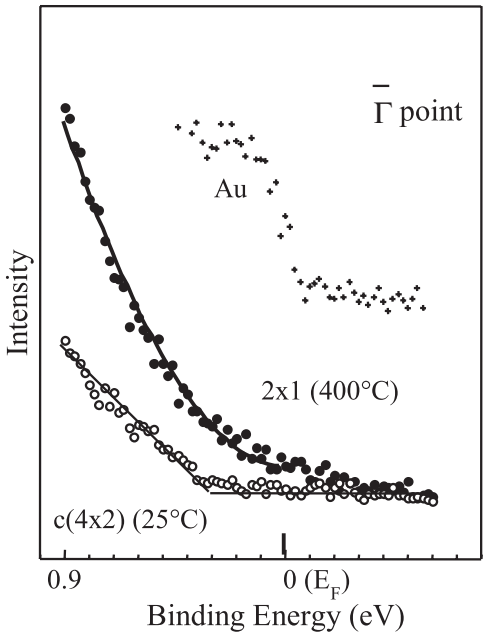

Figure 25. Photoemission spectra near the Fermi level of the Si-terminated β-SiC(100) surface recorded at 25 °C (c(4 × 2)) and 400 °C (2 × 1) at the Γ point. The data have not been smoothed. The solid line represents the best fit obtained for the spectrum at 400 °C with a power-law dependence having a 1.9 exponent. The spectral response of a gold foil is also displayed. The photon energy is $h\nu = 18.9$ eV.

between surface atom electronic orbitals, and favour the metallic character of this surface as observed both by HT-STS (figure 24) and valence band photoemission [38, 83]. Incidentally, one should remark that this temperature-induced c(4 × 2) ⇔ 2 × 1 reversible phase transition cannot be satisfactorily explained by the MRAD model proposed on the basis of total energy calculations [45]. Indeed, in the latter case, it is necessary to infer an increase in the Si coverage when the temperature is raised [45]. Independently from the fact that these calculations are performed at 0 K [45], it is experimentally well known that increasing temperatures result instead in the decrease of the Si coverage at the surface by desorption [35]. Figure 26 displays a schematic diagram of this temperature-induced semiconducting c(4 × 2) ⇔ metallic 2 × 1 reversible phase transition [38].

5. Atomic control and self-organized Si and C nanostructures on β-SiC(100)

5.1. Highly stable 'massively parallel' Si atomic lines and Si dimer chain vacancies

The actual trend in microelectronics is towards much higher integration densities with a road map suggesting a doubling every 18 months (Moore law). However, some serious limitations in this top-down approach are appearing in the near future, raising very fundamental questions. Another approach, the so-called bottom-up approach, would be to manufacture desired patterns by assembling atoms one-by-one using, for example, STM manipulations [84–86]. However, such methods require very long processing times to achieve nanostructures having the desired

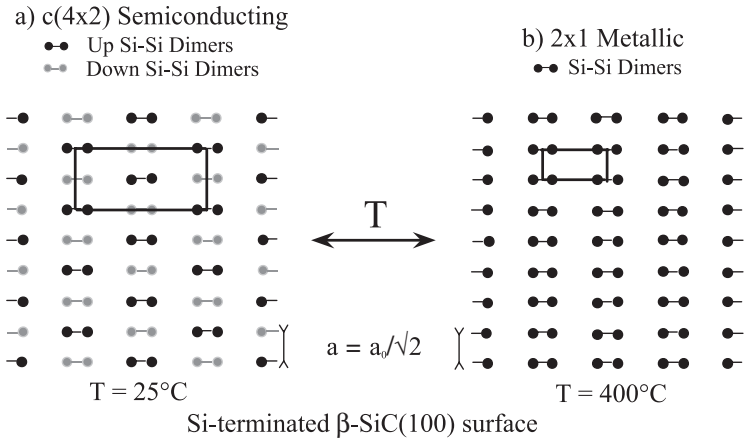

Figure 26. A schematic diagram of the reversible β-SiC(100) surface phase transition from a semiconducting c(4 × 2) reconstruction having dimer rows of up- and down-dimers (AUDD) to a 2 × 1 metallic one having all dimers at the same height. The corresponding surface unit cells are also indicated.

properties and, to limit surface diffusion, low temperatures [84, 85]. This means that, as soon as the surface is warmed up, e.g. to room temperature, atom surface diffusion will destroy the obtained nanopattern. As has been adequately mentioned in the 1999 White House National Nanotechnology Initiative [87], there are some important questions, such as:

(i) What new and novel properties will be enabled by nanostructures *especially at room temperature*?
(ii) What are the surface reconstructions and atom rearrangements in nanorods and nanocrystals?
(iii) Can one extensively use self-assembly techniques to control nanoscale component relative arrangements?

It is interesting to correlate these questions to the recent discovery of Si atomic line formation at the surface of silicon carbide. These lines are self-organized upon temperature-induced β-SiC(100) 3 × 2 surface dismantling, at the phase transition between the Si-rich 3 × 2 and Si-terminated c(4 × 2) reconstructions, and have characteristics that remain unprecedented [7, 13, 14, 17]. One can see in figure 27 that the β-SiC(100) 3 × 2 surface (figure 27(a)) has dramatically changed after thermal annealing at 1050 °C and now exhibits on each terrace a network of long dimer row lines that are separated by ≈19 Å (figure 27(b)) [29]. These Si atomic lines are derived from the dimer rows through the dismantling of the 3 × 2 surface by selective Si atom removal. The resulting pattern corresponds to a 7 × 2 surface reconstruction that could be observed by LEED with a small area having a 5 × 2 array (figure 27(b)) [29].

When the surface is annealed at a slightly higher temperature of 1100 °C, one can see that the spacing between Si atomic lines increases, which results in the decrease of the line density (figure 27(c)). With additional annealings at 1150 °C, one can achieve a surface having a single isolated atomic line (figure 27(d)), with a distance of 400 Å between the two main atomic lines (middle and top right-hand corner of figure 27(d)). The surface between these lines seen in figures 27(c) and (d) exhibits the characteristic pseudo-hexagonal pattern of the c(4 × 2) surface reconstruction [28], indicating that these nanostructures are lying on the Si-terminated surface [29]. One should notice that these lines are very long, with lengths greater than

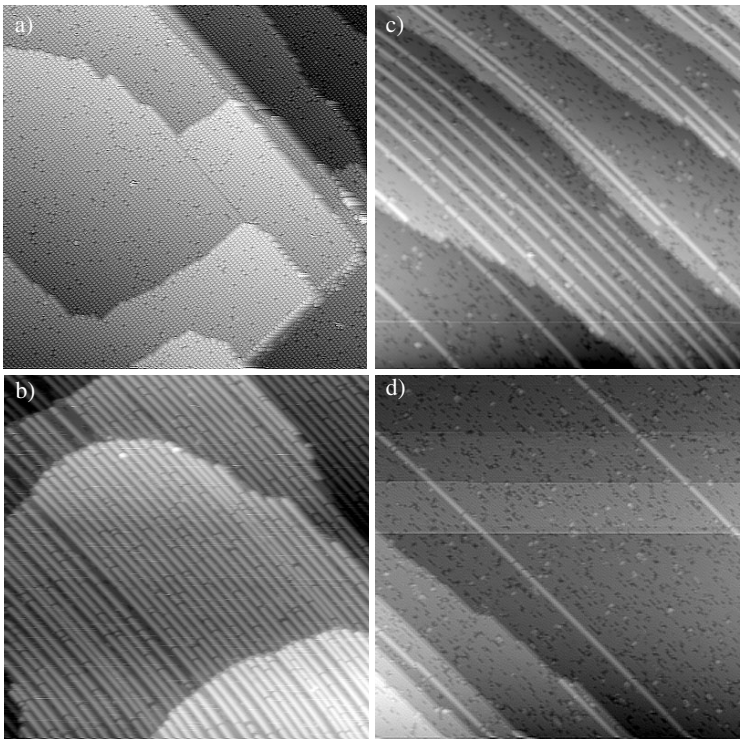

Figure 27. 800 Å × 800 Å STM topographs (filled electronic states) of β-SiC(100) surfaces after annealing. (a) A β-SiC(100) 3 × 2 surface after annealing at 1000 °C. (b) Si atomic lines forming a superlattice obtained after annealing at ≈1050 °C. (c) Si atomic lines obtained after annealing at ≈1100 °C. (d) Isolated single Si atomic lines lying on the β-SiC(100) c(4 × 2) surface obtained after annealing at $T \leqslant 1150$ °C. The two top atomic lines are separated by 400 Å. The tip bias was $V_t = +3.0$ V at a 0.2 nA tunnelling current.

1100 Å (figures 27(c) and (d)) and that their length is limited only by the size of the substrate, since all these Si atomic lines are stopped only at the step edges [29]. In addition, figures 27(a)–(d) indicate that these lines are (i) very long with a length limited only by the substrate, (ii) very stable since high-temperature annealings (>1000 °C) are necessary to remove them, and (iii) the density/spacing of these Si atomic lines could be mediated by a single process, thermal annealing, resulting in arrangements ranging from a single isolated Si line (figure 27(d)) to a superlattice of 'massively parallel' Si atomic chains—see in figure 27(b) [8, 29, 36, 88–90]. At the very beginning of the β-SiC(100) 3 × 2 surface dismantling, one can see in figure 28(a) that the Si atoms are removed dimer row by dimer row, leaving very long Si dimer vacancy lines in the middle of a 3 × 2 surface [89].

Using a very rigorous protocol in surface preparation, it is also possible to prepare defect-free Si dimer lines as shown in a representative STM topograph (figure 25(b)) [89]. In order to identify the atom position in these lines, it is necessary to image the surface by tunnelling into the empty electronic states. In order to correlate filled and empty topographs, we also performed dual scan STM imaging. Figures 29(a) and (b) provide a comparison between empty and filled electronic state topographs of the same atomic lines [89, 90]. One can clearly see in the empty electronic state topograph (figure 29(b)) that, by tunnelling into Si dangling bonds, the lines are made of pairs atoms forming the Si–Si dimers observed in the filled state topograph [89]. Figure 29(c) displays the height profile along XX' corresponding to

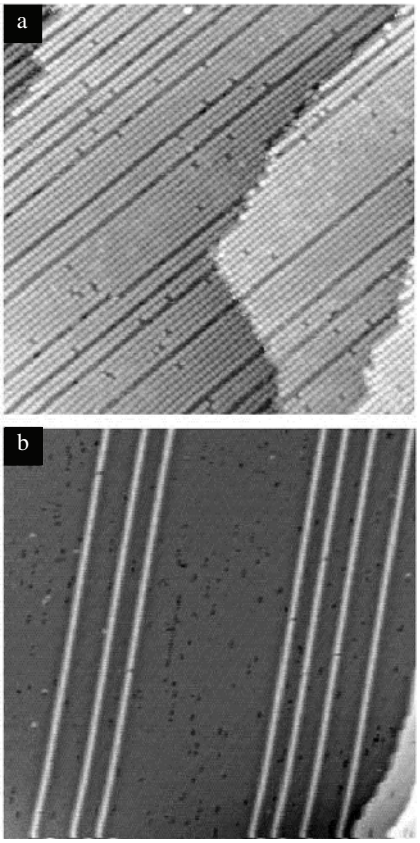

Figure 28. (a) 525 Å × 525 Å STM topographs of a β-SiC(100) 3 × 2 exhibiting dimer row vacancies after a short annealing at 1050 °C. (b) 800 Å × 800 Å STM topographs of a β-SiC(100) silicon-terminated surface presenting isolated silicon lines on top of the c(4 × 2) surface reconstruction. The tip bias was $V_t = 3$ V (filled electronic states) with a tunnelling current of 0.2 nA.

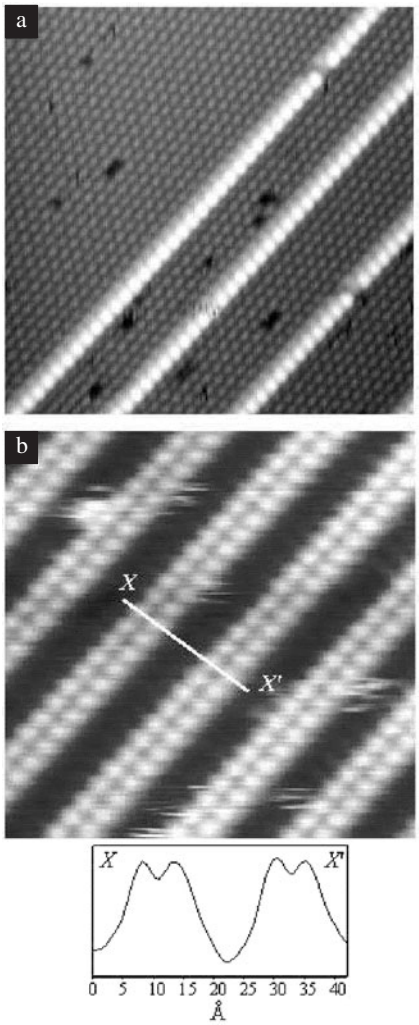

Figure 29. (a) Filled electronic states STM topograph (175 Å × 175 Å) and (b) empty electronic states STM topograph (125 Å × 125 Å) of Si atomic lines on the β-SiC(100) surface. An intensity plot from (b) perpendicular to two atomic lines is also displayed, and shows the symmetric nature of the Si–Si dimers in an atomic line, unlike the case of the dimer rows of the 3 × 2 surface reconstruction.

the empty electronic state STM topograph of Si atomic lines in figure 29(b). One can clearly see that the Si–Si dimer is symmetric [89], unlike the corresponding behaviour of the 3 × 2 surface reconstruction, where dimers forming rows are asymmetric as shown above [27]. This indicates that, when the 3 × 2 surface is dismantled by Si atom thermal removal, the spacing between dimer rows increases, which reduces the lateral interaction.

Another possible interesting ordering configuration is to have these atomic lines self-assembling by pairs in a very particular 8 × 2 array that are imaged by filled and empty STM topographs in figures 30(a) and (b) respectively [36]. The corresponding height profiles also

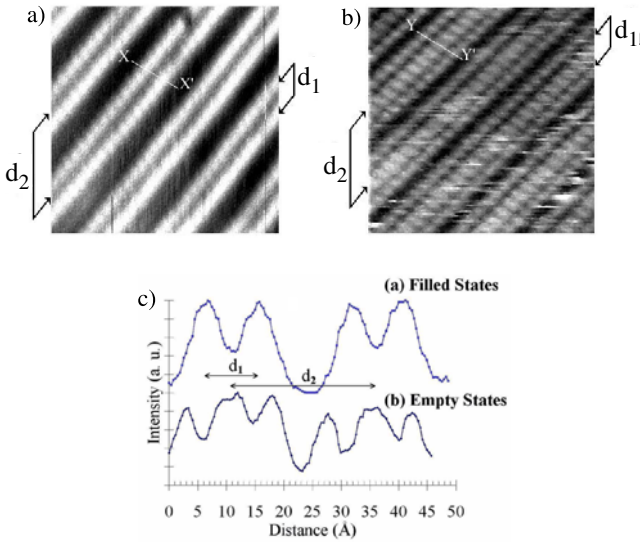

Figure 30. A 100 Å × 100 Å filled electronic state STM topograph of Si atomic line pairs on β-SiC(100). The intra-pair distance d_1 represents the lateral row-to-row distance within an atomic lines pair. The inter-pair distance d_2 represents the distance between the centres of two neighbouring atomic line pairs. The tip bias was $V_t = +3.55$ V at a current $I_t = 0.33$ nA. (b) A 100 Å × 100 Å empty states STM topograph of Si atomic line pairs on β-SiC(100). The tip bias was $V_t = -2.75$ V and current $I_t = 0.33$ nA. d_1 and d_2 are same as in (a). (c) Height profiles covering two line pairs along (a) XX' (filled states) and (b) YY' (empty states).

shown in figure 30 indicate that the dimers are indeed symmetric [36]. This particular 8 × 2 array takes place at the phase transition between the 3 × 2 (Si-rich) and the 5 × 2 (equidistant Si atomic lines) surface reconstructions.

Since these Si atomic lines have their lengths limited by the width of steps, it is challenging to explore if one can build extremely long atomic lines on very large terraces. Most interestingly, figure 31 shows spectacular self-assembled Si atomic lines on such very large terraces. One can see that they are forming a network of massively parallel lines having a length reaching the μm scale (with ≈5000 Si atoms perfectly aligned), and probably much longer [90]. This achievement results in probably what are the longest atomic lines ever built on a surface [90]. The mechanisms involved in these Si dimer line formation is likely to include surface stress reduction. Indeed, when the Si-terminated β-SiC(100) c(4 × 2) surface is covered by an excess of Si atoms, the system tend to have a maximum area of the surface free of Si atoms in excess of the 1 ML Si coverage, in order to favour the AUDD arrangement described above. The best way to achieve this goal is probably to have the Si atoms arranging in dimer lines on top of the c(4 × 2) surface along the Si dimer rows forming the AUDD arrangement [28, 29]. So surface stress is likely to be an important parameter in the formation of these self-organized Si atomic lines [29]. Notice that with the exception of one theoretical calculation for the 5 × 2 Si atomic line array performed in the framework of the MRAD model only [91], there is so far no experimental structural determination of the bonding configuration of these Si dimer lines to the β-SiC(100) c(4 × 2) surface.

5.2. High-temperature dynamics and dismantling of Si atomic lines

In order to explore the stability of these atomic lines, to study their dynamics and to reach the threshold of their dismantling, high-temperature STM experiments were performed [88].

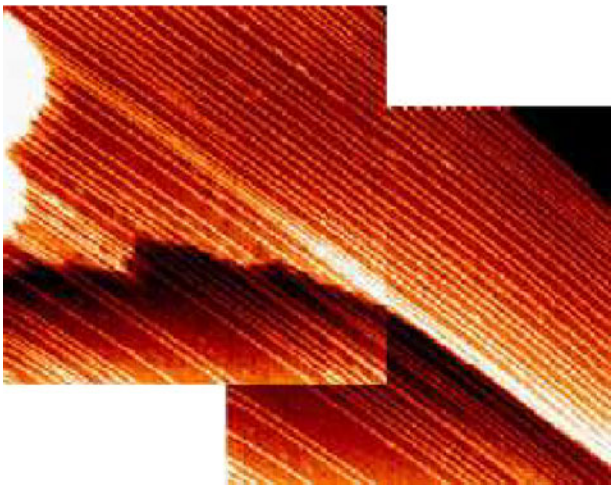

Figure 31. Imaging very long Si atomic lines on a large β-SiC(100) surface: two assembled 2000 Å $\times$ 2000 Å filled electronic state STM topographs. The tip bias was $V_t = -3.0$ V at a tunnelling current $I_t = 0.3$ nA. This gives atomic lines having lengths greater than 0.4 μm and probably much longer since the data acquisition was limited by the scanning capabilities of the AFM/STM instrument used here. These atomic lines, which form a network of 'massively parallel' chains, are probably the longest ones ever built on a surface.

Figure 32 exhibits a series of atom-resolved STM topographs (filled electronic states) recorded at surface temperatures ranging from 25 to 925 °C [88]. As can be seen from figure 32, these Si atomic lines are stable at 600 and 700 °C with none of them broken at such high temperatures [88]. At 700 °C, they are regularly spaced, while the situation seems to change at 800 °C: although almost all dimer lines are still not broken, one can see some gradual changes with very few vacancy segments and an apparent higher line density at the step edge. The latter feature indicates that atomic lines move one-by-one perpendicularly to the line direction and are probably eliminated in a collective mechanism at the step edge. When the temperature is raised to 850 and 900 °C (figure 32), one can observe that the atomic lines are 'sizzling', probably due to the large stress resulting from increasing temperatures, but it is also possible that such high temperatures might correspond to the STM instrumental limitation at these very high temperatures. Anyway, one can clearly notice that the atomic Si lines are still not broken. When the surface temperature is raised by 25 °C, to 925 °C, one can observe that the threshold of temperature-induced atomic line dismantling has been reached, with only few lines remaining and Si island formation taking place [88]. This means that at 925 °C, the Si atom back bonds are broken, leading to Si surface migration with island formation. This further shows that the bonding of the Si dimers with the silicon carbide substrate is very strong; together with a strong dimer–dimer interaction along the atomic line, they are at the origin of their unprecedented stability. Incidentally, these STM experiments represent the highest temperature atom-resolved imaging. Subsequently, and as far as we know, they also show what is probably the highest temperature stability ever achieved for nanostructures built on a surface [88].

Let us now look at the temperature-induced dynamics. Figure 33 displays a series of STM topographs (filled electronic states) for the same area of Si atomic lines; these were recorded for 25 min at a 800 °C fixed temperature [88]. We follow with time the behaviour of an atomic segment line (AS) and a vacancy segment (VS) indicated by an arrow in figure 33, which

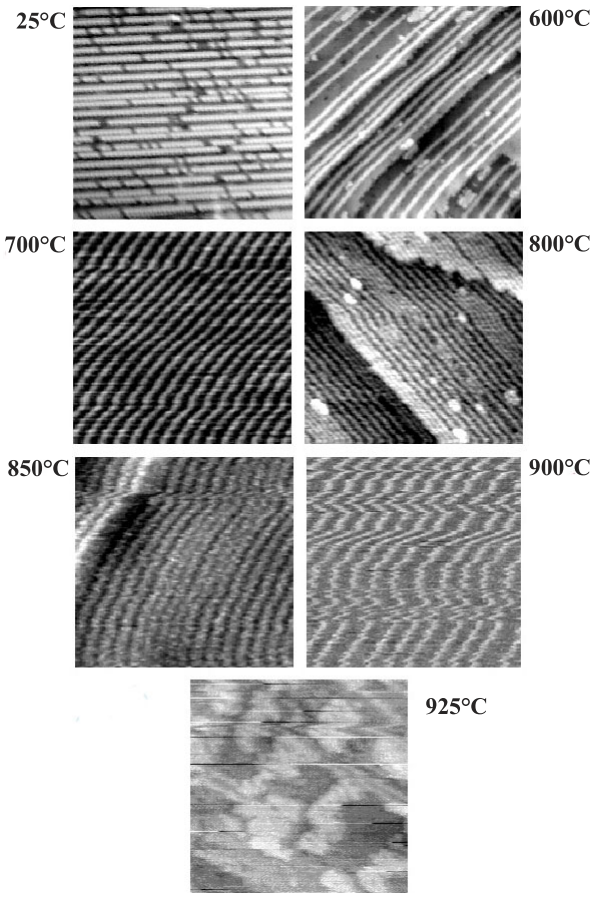

Figure 32. 300 Å × 300 Å STM topographs of Si atomic dimer lines on the β-SiC(100) surface, imaged at temperatures ranging from 25 to 925 °C. Note that, due to the thermal drift, these topographs do not necessarily corresponds to the same area of the surface. At 800 °C, one can already notice the variations in line density, in particular at the step edge.

displays such a sequence. We have eight representative STM topographs (a)–(h) of the same 300 Å × 300 Å area, all recorded at 800 °C. As landmarks to follow the evolution of the same measurement, two defects D1 and D2 are used and keep the same position with the atomic line density remaining about the same except for one, labelled XX' which is of particular interest. The latter, located between D1 and D2, appears to be discontinued with two atomic segments labelled AS 1 (9 dimers) and AS 2 (8 dimers) separated by a vacancy segment VS ($\approx$5 missing dimers) (figure 33(a)), the distance between two dimers along an Si line being 6.16 Å. AS 1, AS 2 and VS evolution with time is followed at a 800 °C constant temperature. In figure 33(b), one can see that, after 3 min, AS 1 and AS 2 exhibit the loss of one and two dimers respectively, with VS becoming longer (7 missing dimers), indicating that AS 2 is also moving away from AS 1, which remains stable. Two minutes later (figure 33(c)), AS 1 shows no change while AS 2 has lost additional dimers, leading to an increased length for the vacancy segment VS by one dimer. At 7 min, AS 2 has only one dimer left, with VS reaching a length corresponding to about 14 missing dimers. This suggests that the remaining AS 2 is still moving away from AS 1 (figure 33(d)). From 8 to 25 min, the last dimer belonging to AS 2 has disappeared,

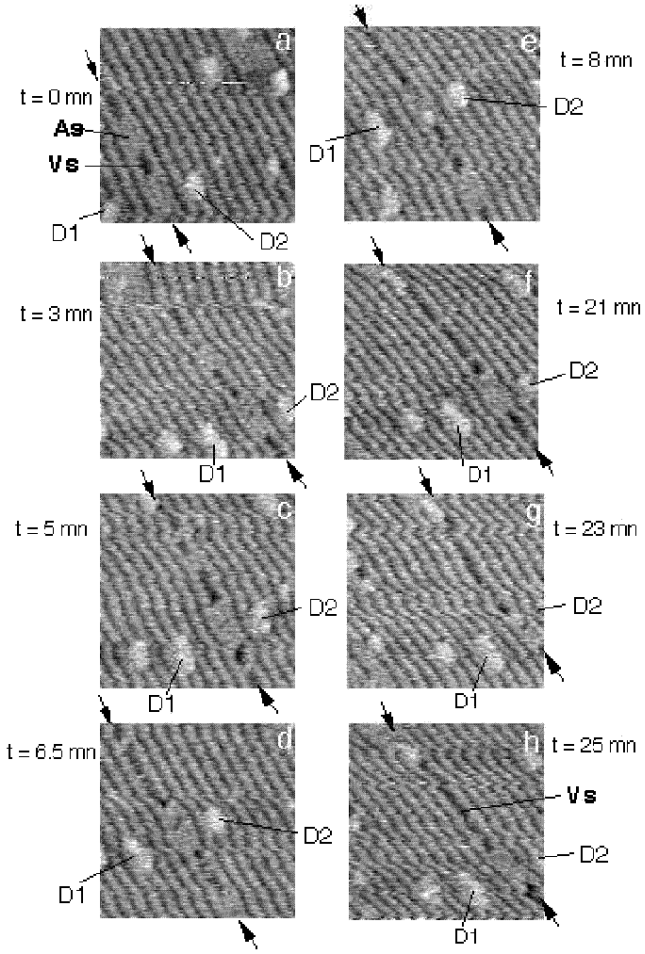

Figure 33. The dynamics of Si dimer lines at fixed 800 °C temperature shown on a series of 300 Å × 300 Å STM topographs. We follow the dismantling with time (from 0 to 25 min) of the Si atomic line marked by arrows into atomic segments (AS) and vacancy segments (VS) ((a)–(h)). Two defects labelled D1 and D2 are used as landmarks to follow the evolution of the same measurement area.

leading to the opening of a much longer vacancy segment VS (>25 missing dimers). This sequence shows that the Si atomic line dismantling also results from an individual mechanism with one-by-one dimer removal [88].

Also, we found that at temperatures above 800 °C, the Si atomic lines move laterally with a higher line density at the step edges. This suggests that the lines are removed one-by-one at the step edges. So the Si thermal elimination on the β-SiC(100) surface results from both individual (one-by-one dimer removal) and collective (line-by-line removal at the step edges) mechanisms [88]. These interesting features are also experimentally advantageous since they probably limit the Si evaporation to the STM tip, therefore making atomic scale STM imaging at such extreme temperatures somewhat easier. Overall, these experiments stress once again the strong interaction between Si dimers belonging to the same line, with this interaction possibly taking place through the SiC surface.

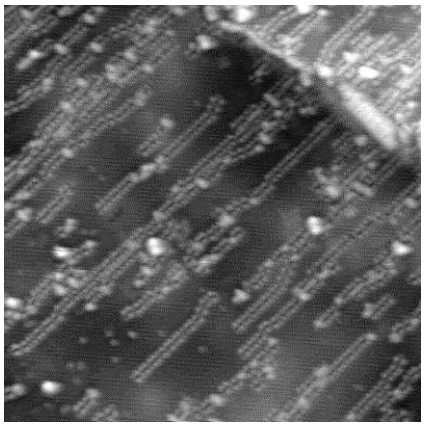

Figure 34. A β-SiC(100) c(2 × 2) surface 600 Å × 600 Å STM topograph (empty electronic states) having C atomic lines. The tip bias was $V_t = -3$ V with a 0.3 nA tunnelling current.

5.3. Carbon atomic chain formation and the $sp \rightarrow sp^3$ diamond type transformation of the β-SiC(100) c(2 × 2) surface

As described above, the C atomic plane on the C-terminated β-SiC(100) c(2 × 2) surface reconstruction is driven by surface stress [34, 46]. Since stress has been shown to be the leading driving force in Si atomic line organization [29], it is especially interesting to explore if one can also build C nanostructures on this β-SiC(100) c(2 × 2) surface. Indeed, the latter has its surface organization driven by anisotropic compressive stress along the dimer rows and tensile stress perpendicular to the dimer rows [34]. It is possible to modify the balance between these two factors by thermal annealing. It is therefore challenging to explore if one can also build C nanostructures on β-SiC(100) surfaces. We first look at the effect of 9 min of annealing at 1250 ± 30 °C on the β-SiC(100) c(2 × 2) surface. Figure 34 shows the corresponding STM topograph (600 Å × 600 Å) which exhibits a large number of nanostructures made of double spot rows oriented perpendicular to the step edge [33]. One can immediately remark that these C atomic lines are very different from the Si atomic lines observed above (figures 27– 31) since the latter are very straight and have their length (>1 μm) limited only by the substrate [29]. Instead, the C atomic lines have lengths ranging from 20 to 400 Å and are not necessarily straight. In addition, while the Si atomic lines are built above the surface, the C atomic lines are part of the surface [33].

Figures 35(a)–(c) show more detailed images of these atomic lines with empty electronic state STM topographs for a β-SiC(100) c(2 × 2) surface after annealing at 1250 °C for 8, 15, and 23 min. One can see that the atomic line density increases with the annealing time to cover the whole surface after 23 min at 1250 °C (figure 35(d)). These atomic lines are made of double spots corresponding to atomic lines made of asymmetric C–C dimers having a single bond in an sp^3 electronic configuration and 2 dangling bonds on each C atom belonging to a dimer [33]. Upon increasing the temperature, the C≡C triple bond dimer is broken, with a 90° rotation leading to the establishing of the simple bond C–C dimer having a diamond-like sp^3 configuration [33]. At longer annealing times, the surface undergoes a diamond-type transformation and is covered by sp^3 C atomic lines.

Additional insights about this diamond-type surface transformation could be found by looking at recent *ab initio* first principles theoretical calculations using the density functional theory (DFT) approach and generalized-gradient approximations (GGA) studying C atomic line formation on the β-SiC(100) c(2 × 2) surface [92]. Interestingly, it is found that, at 0 K, the formation of sp C≡C triple bond dimers (c(2 × 2) reconstruction) is favoured

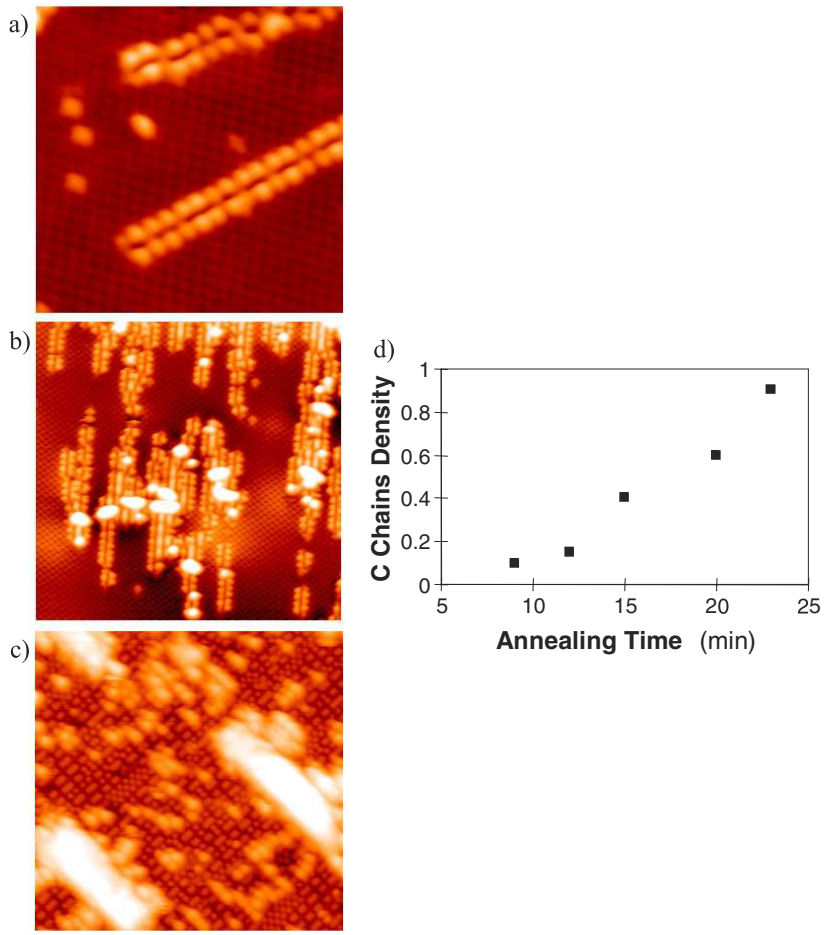

Figure 35. 300 Å × 300 Å STM topographs of a C-terminated β-SiC(100) c(2 × 2) surface obtained by tunnelling into (a) the empty and (b) the filled states after a 15 min annealing the surface at 1250 °C. 200 Å × 200 Å STM topographs obtained by tunnelling into (c) the empty electronic states and (d) the filled electronic states after a 23 min annealing at 1250 °C. One can clearly see the growth of sp^3 diamond-like atomic lines. The density of these C chains versus annealing time at 1250 °C is provided in (d). The tip bias was $V_t = \pm 3$ V at a 0.3 nA tunnelling current.

over sp^3 C–C simple dimers by only a few millielectronvolts per dimer [92]. However, for small applied compressive stress geometries, the situation is reversed, favouring a sp^3 bonding configuration [92]. This means that, in the real experimental situation, when the temperature is raised to around 1250 °C, the situation is most likely reversed, favouring sp^3 defect formation [92]. Most significantly, as soon as the number of sp^3 defects increases, the energy to form an additional sp^3 defect decreases drastically, leading to the formation of sp^3 C–C dimer lines [92]. Also, the sp^3 C–C dimer is slightly below the surface (by 0.3 Å), which is in agreement with the above STM observation that this sp^3 C–C dimer is 'within' the c(2 × 2) surface, since the STM does probe electronic 'heights' rather than geometric ones. In addition, the calculated STM images [92] are found to be in excellent agreement with the experimental STM topographs, as can be seen in figure 36. In particular, experimental and calculated height profiles show the asymmetric nature of the sp^3 C–C dimer at low coverages [33, 92].

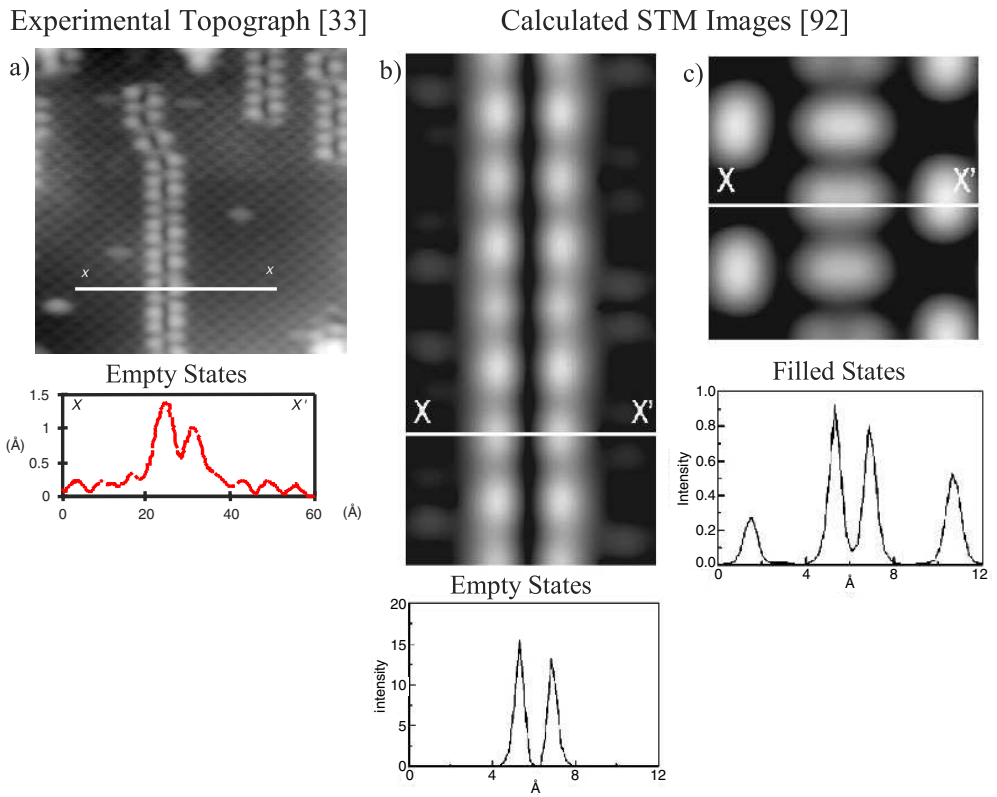

Figure 36. Comparison between an experimental STM topograph and a calculated STM image for sp^3 C–C dimer lines on the β-SiC(100) c(2×2) surface: (a) 100 Å × 100 Å STM topographs (empty electronic states) with a straight C atomic line and a C atomic line with a bend. A height profile along an sp3 C–C dimer (XX') and perpendicular to sp C≡C dimer bonds is provided at the bottom [33]. Calculated empty (b) and filled (c) electronic states STM images for the β-SiC(100) c(2 × 2) surface with a sp^3 defect concentration of 1/2 with corresponding height profiles along an sp^3 C–C dimer and perpendicular to sp C≡C dimer bonds. The images are computed with a constant current [92]. Notice the agreement between the STM topograph and the calculated image showing the asymmetric nature of the sp^3 C–C dimer line when isolated.

It is very interesting to remark that such a diamond-type transformation takes place in vacuum and temperature conditions that are very close to those of diamond growth in interstellar space and which are found, for example, on meteorites [9]. Figure 37(a) gives a model of the sp to sp^3 diamond-type transformation with atomic C lines made of asymmetric dimers at low line density, when the spacing between these sp^3 line is large [33]. When these lines cover the whole surface, the interaction between two sp^3 dimers belonging to adjacent lines leads to symmetric C–C dimers as depicted in figure 37(b).

6. Nanochemistry on β-SiC(100) surfaces

6.1. Molecular hydrogen interaction with the 3 × 2 *and* $c(4 \times 2)$ *reconstructions*

Since the surfaces of cubic silicon carbide could now be considered as well-defined with identification of their atomic structure, it is interesting to look at the effect of some simple adsorbate like hydrogen on both molecular and atomic species. Hydrogen interaction with

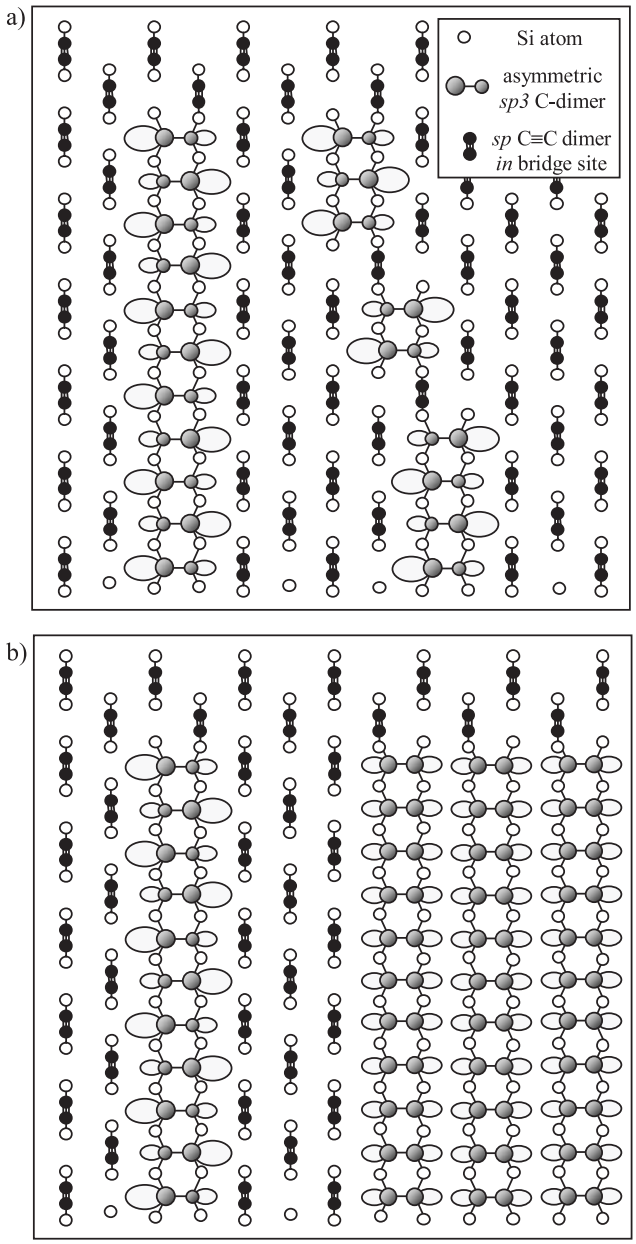

Figure 37. A schematic display of the structure of (a) a straight C atomic line (left) and (right) another one showing a detailed scheme of a C line bend, with in both cases asymmetric C–C dimers. When the C atomic chain density increases, the C–C dimers become symmetric as shown in (b). The surface primitive unit cell parameter is $a = a_0/\sqrt{2}$ where $a_0 = 4.36$ Å is the β-SiC lattice constant.

silicon surfaces has been shown to result in very efficient surface passivation [93, 94]. So it is challenging to investigate the effect of molecular hydrogen on SiC. We look at the effect of H_2 on the cubic Si-rich 3×2 [27] and Si-terminated c(4×2) β-SiC(100) [28] surface

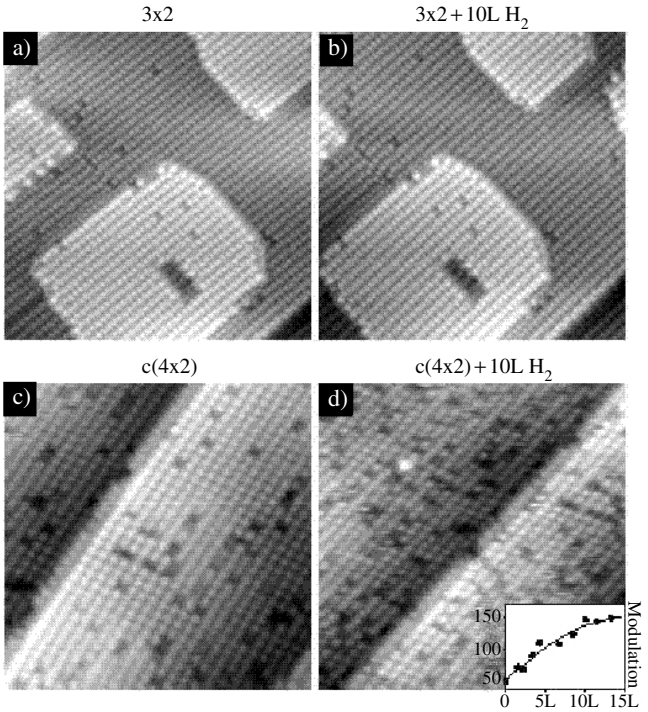

Figure 38. (a) and (b) H_2/β-SiC(100) 3×2: 300 Å $\times$ 300 Å STM topographs (filled states) of clean (a) and 10 L exposed surface (b). (c) and (d) H_2/β-SiC(100) $c(4 \times 2)$: 200 Å $\times$ 200 Å STM topographs (filled states) of clean (c) and 10 L H_2 exposed surface (d). The number of H adsorption sites versus H_2 exposures is also displayed in (d).

reconstructions using STM. Figures 38(a)–(d) display STM topographs for clean and 10 H_2 L exposed 3×2 and $c(4 \times 2)$ surfaces. One can clearly see that, while the β-SiC(100) 3×2 exhibits no change upon H_2 exposure, the β-SiC(100) $c(4 \times 2)$ surface is significantly affected, with new dark spots indicating hydrogen interaction with up-dimers [95]. Such a reaction implies H_2 dissociation. The inset in figure 38(d) displays a plot representing the number of dark sites versus H_2 exposures. From the initial slope, one can derive the RT molecular H_2 sticking probability on the β-SiC(100) $c(4 \times 2)$ surface as $s_0 = 2 \times 10^{-3}$ [95]. Interestingly, this value is very high, especially when compared to the Si(100) surface, where H_2 sticking probabilities are $s_0 < 1 \times 10^{-11}$ for terraces [96], i.e. 8 orders of magnitude higher. In the empty states topographs, each spot corresponds to a down Si–Si dimer of the AUDD model [28]. While the H atoms interact with up-dimers, this affects the two down-dimer nearest neighbours belonging to the same row with a significant charge redistribution [95].

The valence band (VB) gives additional insights about H_2 on β-SiC(100) surfaces. Figure 39 displays representative VB spectra for clean and H_2 covered 3×2 (a) and $c(4 \times 2)$ (b) surfaces. Both clean surfaces exhibit bulk (B) and surface (S_a and S_b) states, the latter ones related to Si–Si dimers and located in the band gap [59, 38]. The β-SiC(100) 3×2 VB spectra show no change with H_2 exposures, further stressing no reaction to H, in excellent agreement with the real space STM surface imaging. Instead, the $c(4 \times 2)$ surface state S_b is rapidly quenched upon H_2 exposures, indicating a strong interaction with the Si dimers, very likely through the dangling bonds. Since STM is tunnelling from the surface states, this behaviour

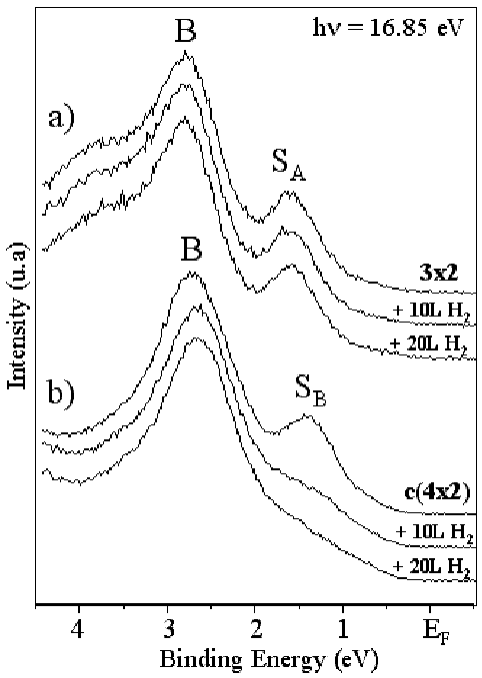

Figure 39. Valence band photoemission spectra ($h\nu$ = 16.85 eV) for clean and H_2 exposed to 10 and 20 L of (a) β-SiC(100) 3×2 and (b) β-SiC(100) $c(4 \times 2)$ surfaces. The photon energy was 16.85 eV (Ne I).

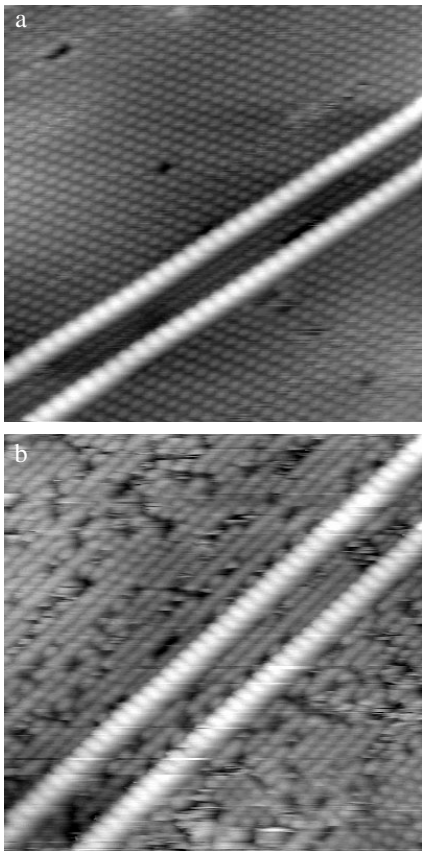

Figure 40. 200 Å × 200 Å STM topographs (filled states) showing the H influence on Si self-organized atomic lines built on a β-SiC(100) $c(4 \times 2)$ surface. One can notice that H reacts with the surface (becoming 2×1) and not with the Si atomic lines which remain unaffected.

explains why reacted H sites appear dark in the filled state topographs. No more VB change occurs at higher H_2 exposures, indicating saturation, while the VB still has a significant density of states below E_F, with a surface exhibiting an H-induced 2×1 array [95, 97], with all dimers being at the same height due to H-induced charge transfer into Si dimers [95].

The above results indicate that H_2 molecules react with up-dimers of the β-SiC(100) $c(4 \times 2)$ surface reconstruction with subsequent dissociation and H atom adsorption on dangling bonds producing a double hydrogenated dimer (monohydride). This behaviour is very different from the Si(100) 2×1 surface, where H_2 dissociation takes place at steps/defects only, the terraces remaining inert at RT ($s_0 \approx 10^{-11}$) [96]. This very different situation between β-SiC(100) $c(4 \times 2)$ and Si(100) 2×1 results from major electronic and structural differences. Indeed, SiC lattice distortions, stressed backbond relaxation and electronic redistribution around E_F play a crucial role in the process, leading to very high sticking probabilities ($s_0 \approx 2 \times 10^{-3}$). The fact that, at low-temperature annealing (700 °C), the hydrogenated surface eliminates the dark reacted spots and restores the $c(4 \times 2)$ surface indicates that these reacted dark sites do not correspond to missing dimers [95]. This also shows that the H

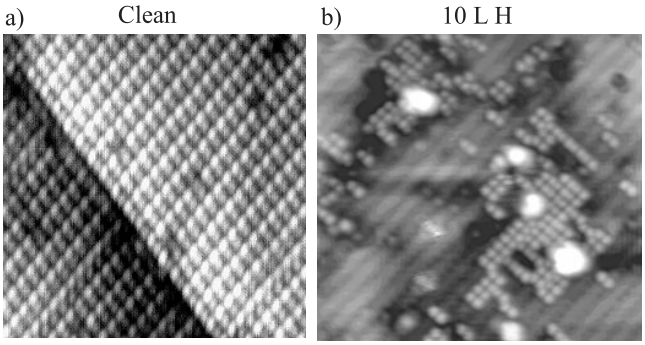

Figure 41. H/β-SiC(100)-3 × 2: 150 Å × 150 Å empty electronic states STM topographs (tip bias −3 V at a 0.2 nA tunnelling current), on clean and 10 L atomic hydrogen exposed surfaces.

interaction does not result in surface etching, with no thermal desorption of Si–H radicals. Therefore, while the β-SiC(100) 3 × 2 surface remains totally inert to molecular hydrogen, the β-SiC(100) c(4 × 2) is highly reactive to H_2 (with sticking probabilities $\approx 10^{+8}$ higher than for silicon), resulting in molecular dissociation. H atoms are adsorbed at Si dangling bond sites, leading to higher exposures to H inducing a 2 × 1 surface as a result of all Si dimers being at the same height [95, 97]. Finally, the Si-terminated β-SiC(100) surface passivation by hydrogen allows Si atomic lines to be built, which like the 3 × 2 reconstruction remain unaffected by molecular H_2, on a passivated wide band gap semiconductor surface, as can be seen in figure 40 [95].

6.2. Atomic hydrogen-induced β-SiC(100) 3 × 2 surface metallization

The passivation of semiconductor surfaces against chemical attacks can be achieved by terminating the surface-dangling bonds with a monovalent atom such as hydrogen. Such passivation leads to the removal of all surface states in the band gap, and thus to the termination of non-metallic surfaces. Such an approach has been especially successful for the Si surfaces [93, 94]. As just seen above, the Si-terminated β-SiC(100) c(4 × 2) surface reconstruction is also decorated by H [95]. Contrary to previous beliefs [64], the Si-rich β-SiC(100) 3 × 2 surface keeps its original 3 × 2 ordering upon atomic H-exposures [65].

The first example of H-induced semiconductor surface metallization is shown to occur on the Si-rich β-SiC(100) 3 × 2 surface [65]. This striking result is established by atom-resolved scanning tunnelling microscopy and spectroscopy (STM, STS), synchrotron radiation-based core level and valence band photoelectron spectroscopies (CL-XPS, VB-UPS) and multiple reflection infrared absorption spectroscopy (MR-IRAS). It was performed for the Si-rich β-SiC(100) 3 × 2 surface. The metallization is evidenced/understood by band gap closing (STS), Fermi level built-up (VB-UPS), Si 2p reactive component (CL-XPS) and specific vibrational features (MR-IRAS). The synchrotron radiation-based photoemission experiments were performed at the third generation Elettra source on the VUV beam line using the Si 2p core level and valence band at a base pressure in the 10^{-11} Torr. Atomic H exposures were performed at a sample temperature of 300 °C using research grade hydrogen dissociated by a heated tungsten filament.

We first look at the effect of atomic H exposures on the surface structure by scanning tunnelling microscopy (STM) and spectroscopy (STS). Figure 41 displays 150 Å × 150 Å STM topographs (empty electronic states) for a clean (1a) and a partially H-covered (1b)

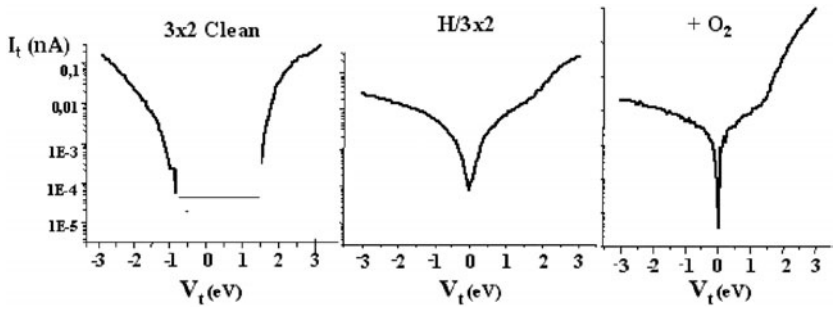

Figure 42. STS $I(V)$ measurements on a clean 3×2 surface (left), on H covered 3×2 (centre) and O_2 exposed (500 L) (right). Upon H atomic exposure, band gap closing occurs, with no band gap opening when the hydrogenated surface is exposed to oxygen.

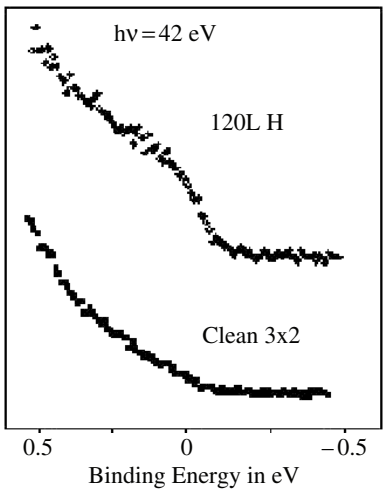

Figure 43. Metallization of the H/β-SiC(100) 3×2 surface evidenced through Fermi level build-up in valence band ultraviolet photoemission spectroscopy using synchrotron radiation at a photon energy of $h\nu = 42$ eV.

β-SiC(100) 3×2 surface. As can be seen from figure 41(a), while the clean surface exhibits the expected asymmetric Si dimers [27, 65], when the surface is exposed to atomic H (figure 41(b)), the H atoms decorate the Si dangling bonds, leading to top Si dimers becoming symmetric and keeping a 3×2 array as for clean surface [65].

Next, we now look at the electronic properties using scanning tunnelling spectroscopy (STS) and at the spectral response around the Fermi level by photoemission spectroscopy. As can be seen from figure 42 which displays the I–V characteristics for clean and H-covered surface, H exposure results in β-SiC(100) 3×2 band gap closing [65]. Such a behaviour suggests surface metallization. Most interestingly, such a metallization does not seem to be affected by oxygen adsorption, since upon a 500 L of O_2 exposure on the hydrogen covered 3×2 surface, STS shows no band gap opening (figure 42, right) [98, 99].

Deeper insight into this interesting H-induced surface metallization can be found by looking at the electronic properties around the Fermi level using valence band photoemission at $h\nu = 42$ eV photon energy. As can be seen from figure 43, the H interaction with the β-SiC(100) 3×2 surface results in a surface state developing at the Fermi level with a clear Fermi edge indicating surface metallization [65, 100].

In order to understand the nature of the hydrogen interaction onto the β-SiC(100) 3×2 surface better, we now use high-energy resolution core level photoemission spectroscopy at the

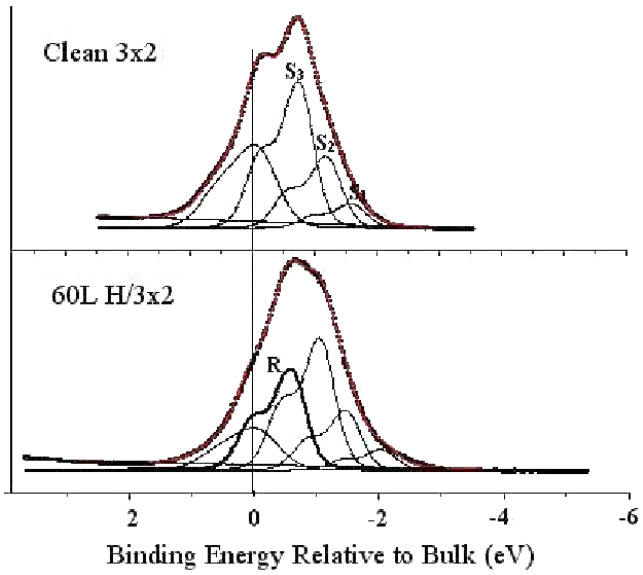

Figure 44. H/β-SiC(100) 3 × 2: Si 2p core level decomposition for clean (top) and H covered (bottom) 3 × 2 surface. S_1, S_2 and S_3 are the surface and subsurface shifted components and R the reactive component. The binding energy reference is relative to B, the bulk component. The photon energy was $h\nu = 150$ eV.

Si 2p core level which provides very useful insights into Si bonding configurations. Figure 44 shows the Si 2p core level recorded at a 150 eV photon energy (surface sensitive mode) for the clean and the H-exposed 3×2 surface reconstruction. The spectra are decomposed into surface, subsurface and bulk components that are specific of the 3 × 2 reconstruction: it includes 3 surface and subsurface shifted components [98, 99]. S1 is related to the up-atom of the top asymmetric dimer. S2 accounts for the down-atom of the top asymmetric Si dimer and to atoms located in the second Si plane. S3 is connected to the Si–Si dimers located in the third Si atomic plane and to the other Si atoms in the second plane that are not related to S2 [98, 99]. The effect of H atoms on surface Si atoms can be traced in figure 44, which shows that S1 is shifted by 450 meV to lower binding energy as a result of charge transfer into the top dimer leading to it being symmetric. Such an energy shift to lower binding energy is also an indication of surface metallization as observed, for example, for III–V compound metal/semiconductor interfaces [24]. The other interesting feature is the appearance of a reacted shifted component R shifted by 470 meV to higher binding energy from the S3 subsurface component. This indicates strong H interaction below the surface, breaking Si dimers in the subsurface region, leaving some Si atoms with very different electronic status than on the clean surface [99]. Indeed, such a behaviour could be correlated to the multiple reflection-infrared absorption spectroscopy (MR-IRAS) experiments showing a specific vibrational mode indicating H atom bonding to an Si atom which is bonded to a C atom [65]. This could occur only in the third Si plane located just above the first C plane—see, for example, figure 10 above [50].

The H atoms attack on the third plane Si–Si dimers leads to dimer breaking, leaving two Si dangling bonds which are expected to become terminated by an H atom just like for the top surface dangling bonds. However, due to steric space limitations, only one Si dimer could be decorated by an H atom, leaving the other one empty [65, 99]. Such an asymmetric attack results in a very different electronic status between the two Si atoms initially forming a

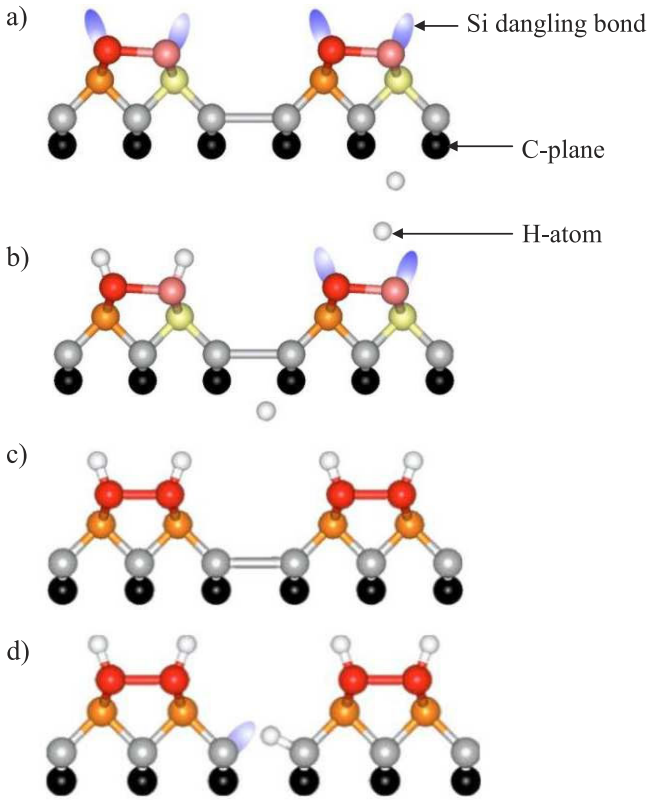

Figure 45. A sequence showing the H atoms interacting with the β-SiC(100) 3 × 2 surface and subsurface: (a) clean β-SiC(100) 3 × 2 surface; (b) impinging H atoms decorate Si dangling bonds; (c) top Si–Si dimers become symmetric, which weakens Si–Si dimers in the third plane; (d) asymmetric attack of H atoms on the Si–Si dimers in the third plane with, due to steric hindrance, only one Si dangling bond being decorated by an H atom. This leads to charge transfer and metallization. As seen above, the β-SiC(100) 3 × 2 surface reconstruction includes three silicon atomic layers (1/3SiML + 2/3SiML + 1Si ML) on top of the first carbon plane—see figure 10.

dimer, leading to a significant charge transfer that induces the observed metallization [65, 99]. Figure 45 displays a sequence of the H atoms interaction with the β-SiC(100) 3 × 2 surface showing the different steps described above. Another interesting aspect of this H-induced metallization is that it originates from atomic defects organized in stripes along an atomically straight line, as can be seen in figure 46 on a 3D view of the hydrogenated surface. Also, H hopping between the two dangling bond sites of the third-layer broken dimer could be expected, due to the small distance between the Si atoms [50], suggesting a possible one-dimensional character of the electronic states responsible for the metallization [65, 100].

This hydrogen-induced β-SiC(100) 3 × 2 surface is in sharp contrast with the behaviour of diamond covered by hydrogen which remains insulating [101, 102]. However, such an H-covered diamond surface becomes conducting when exposed to air, likely due to the doping effect of water [102]. Notice that, very recently, deuterium has also been found to induce conductivity on a diamond boron-doped surface [103]. In the latter case, the mechanism seems to be very different from the H-induced SiC metallization [65] since it is also related to a doping effect. Indeed, the deuterium-induced diamond conductivity results rather from

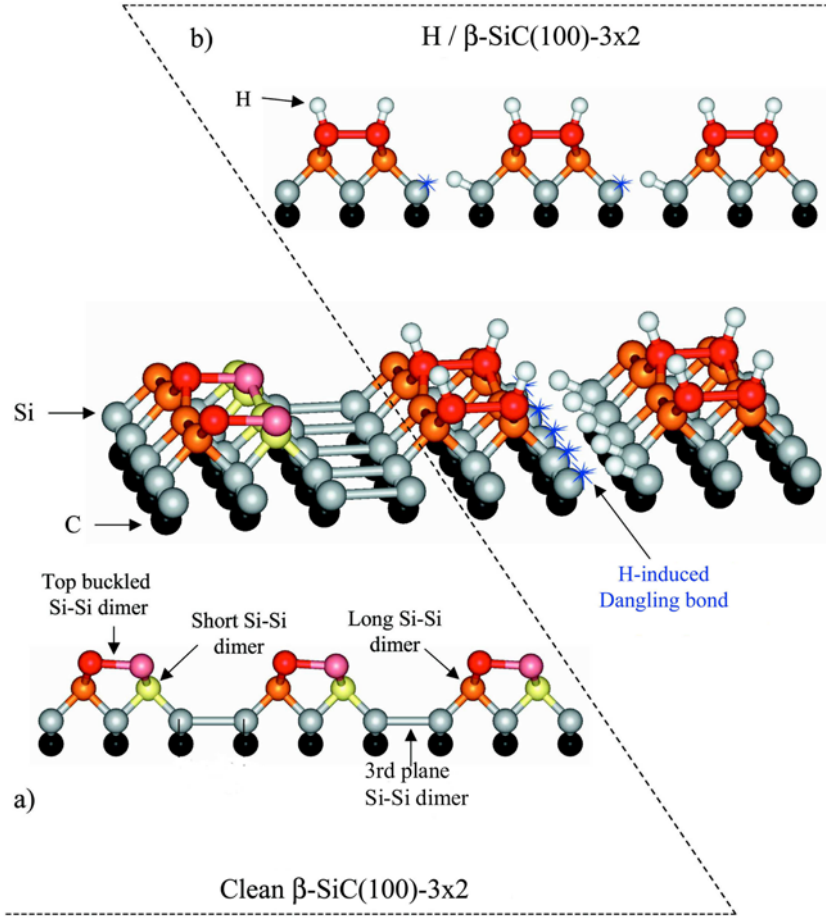

Figure 46. Schematic atomic models (side and 3D views) of the clean and H-covered β-SiC(100) 3 $\times$ 2 surfaces: (a) clean and (b) H-covered. The atomic structure of the clean β-SiC(100) 3 $\times$ 2 surface was determined by real space atom-resolved STM [27], theory [62] and grazing incidence x-ray diffraction [50].

deuterium diffusion through the entire boron-doped layer, leading to the passivation of boron acceptors with a conversion from a highly p-type status to an n-type conductivity [103].

To conclude this section, atomic hydrogen deposition on the Si-rich β-SiC(100) 3 $\times$ 2 surface is found to induce surface metallization, which is the first example of H-induced semiconductor surface metallization [65]. This unprecedented feature results from H inducing an asymmetric attack on the subsurface Si–Si dangling bonds, creating a specific defect. The metallization process results from the competition between hydrogen termination of surface dangling bonds and hydrogen-generated steric hindrance below the surface. Most interestingly, the H/β-SiC(100) 3 $\times$ 2 surface does not seem to be very sensitive to corrosion since its metallization is not removed by oxygen. The hydrogen-induced metallization directly impacts the ability to eliminate electronic defects at semiconductor interfaces critical for microelectronics, provides means to develop electrical contacts on high band-gap chemically passive materials, particularly exciting for interfacing with biological systems, and gives control of surfaces for lubrication, e.g. of nanomechanical devices.

7. Conclusions, new developments and perspectives

We have reviewed the atomic structure and properties of the (100) face of cubic β-SiC surface reconstructions, Si atomic lines self-formation, temperature-induced metallic phase transition, diamond type surface transformation and nanochemistry with the unprecedented finding of H-induced semiconductor surface metallization. These have been established using advanced experimental techniques such as atom-resolved scanning tunnelling microscopy and spectroscopy, synchrotron radiation-based valence band and core level photoelectron spectroscopies and grazing incidence x-ray diffraction, and by *ab initio* total energy calculations. Overall, the knowledge and understanding of β-SiC(100) surfaces has made considerable progress during the last decade, showing the existence of many surface reconstructions, the formation of Si or C nanostructures having unprecedented characteristics, exotic phase transitions and novel nanochemistry. SiC is a model system, and as appropriately mentioned by Bermudez [47], appears as a 'surface science laboratory' on its own. Its surface can now be controlled at the atomic scale and exhibits very complex reconstruction structures that are often driven by stress. Knowledge, atomic scale control and understanding of the surfaces of this advanced material now open up the possibility to investigate adsorbates, interfaces and novel nanostructures of this model semiconductor and address new issues of both fundamental and technological importance.

Acknowledgments

This work was developed and performed at the Commissariat à l'Energie Atomique, Saclay, France, in the Laboratoire SIMA. The authors are especially grateful to their collaborators, including M D'angelo, V Yu Aristov, V Derycke, L Douillard, P Fonteneau, N P Pham, F Semond and M Silly. They also want to acknowledge gratefully collaborations in synchrotron radiation with G Renaud and A Barbier at CEA and ESRF (Grenoble, France), G Le Lay at Université de Provence (Marseille, France), A Cricenti, C Crotti, C Ottaviani, M Pedio and P Perfetti at CNR (Rome, Italy) and Elettra (Trieste, Italy), C Grupp and A Taleb-Ibrahimi at Lure (Orsay, France). They also thank G Dujardin, A Mayne and the Laboratoire de Photophysique Moléculaire at CNRS (Orsay, France) for the use of their STM on which part of the initial measurements were carried out, and F Amy and Y Chabal at Agere/Bell Labs (Murray-Hil, NJ, USA) for performing the IRAS experiments on the H/β-SiC. On the theoretical side, very useful collaborations with E Wimmer at Materials Design (Le Mans, France), G Galli at the Lawrence Livermore National Laboratory, Department of Energy (Livermore, CA, USA), A Catellani (CNR, Parma, Italy), and with V Aroutiounian and V Buniatian at the Yerevan State University (Armenia) are gratefully acknowledged. Finally, such experiments would not have been successful without having high-quality β-SiC(100) thin films provided by Th Billon, L di Cioccio, C Jaussaud and C Pudda at CEA-LETI (Grenoble, France), A Leycuras at CNRS-CRHEA (Sophia-Antipolis, France) and V Monteil at Université Claude Bernard, (Lyon, France). Finally PS wishes to thank W J Choyke for sharing his tremendous experience and vision of this fascinating material.

References

[1] Berzelius J J 1824 *Ann. Phys., Lpz.* II **5** 209
[2] Acheson E G 1891 *J. Franklin Inst.* 194
[3] Moisan H 1904 *C. R. Acad. Sci.* **139** 773

[4] Choyke W J, Matsunami H M and Pensl G (ed) 1998 *Silicon Carbide, a Review of Fundamental Questions and Applications to Current Device Technology* vol 1 and 2 (Berlin: Akademie) and references therein
[5] 1997 Silicon carbide electronic devices and materials *Mater. Res. Soc. Bull.* **22** and references therein
[6] 1999 *IEEE Trans. Electron Devices* **46** (Special issue on silicon carbide electronic devices) and references therein
[7] 1998 Diamond detector devices and materials *Mater. Res. Soc. Bull.* **23** (September) and references therein
[8] Soukiassian P and Semond F 1997 Surfaces and interfaces of advanced materials *J. Physique* IV **7** 10 and references therein
[9] Soukiassian P and Dujardin G 1999 *La Recherche* **321** 38 and references therein
[10] Bechstedt F, Fissel A, Grossner U, Kaiser U, Weissker H C and Wesch W 2002 *Mater. Sci. Forum* **389–393** 737
[11] Aroutiounian V M, Bouniatian V V and Soukiassian P 1999 *Solid. State Electron.* **43** 343
[12] Asriyan H V, Gasparyan F V, Aroutiounian V M and Soukiassian P 2001 *Appl. Surf. Sci.* **184** 460
[13] Buniatian V V, Gasparyan F V, Aroutiounian V M and Soukiassian P 2001 *Appl. Surf. Sci.* **184** 466
[14] Gasparyan F G, Aroutiounian V M and Soukiassian P 2002 *World Renewable Energy* ed A A M Sayigh (Amsterdam: Elsevier Science) p 40
[15] Lely J A 1955 *Ber. Deut. German. Ges.* **32** 229
[16] Tairov Yu M and Tsvetkov V F 1978 *J. Cryst. Growth* **43** 209
[17] see e.g. Nishino S 1995 *Properties of Silicon Carbide* (*EMIS Datareview Series* vol 13) ed G Harris (London: INSPEC) p 204 and references therein
[18] Pons M and Madar R 2004 *J. Phys.: Condens. Matter* **16** and references therein
[19] Dudley M, Huang X, Vetter W M and Neudeck P G 2003 *Materials Science Forum* vol 433–436, ed P Bergman and E Janzén (Switzerland: TransTech) p 247
[20] Leycuras A 1997 *Appl. Phys. Lett.* **70** 1533
[21] Ferro G and Monteil Y 2000 *Le Vide-Science, Technique et Applications* **298** 406 (Special issue on silicon carbide (in French))
[22] Duke C B 1996 *Chem. Rev.* **96** 1237 and references therein
[23] Kubby J A and Boland J J 1996 *Surf. Sci. Rep.* **26** 63 and references therein
[24] Mönch W 1993 *Semiconductor Surfaces and Interfaces* (Berlin: Springer) and references therein
[25] LaFemina J P 1992 *Surf. Sci. Rep.* **16** 133 and references therein
[26] Bermudez V M 1997 *Phys. Status Solidi* b **202** 447 and references therein
[27] Semond F, Soukiassian P, Mayne A, Dujardin G, Douillard L and Jaussaud C 1996 *Phys. Rev. Lett.* **77** 2013
[28] Soukiassian P, Semond F, Douillard L, Mayne A, Dujardin G, Pizzagalli L and Joachim C 1997 *Phys. Rev. Lett.* **78** 907
[29] Soukiassian P, Semond F, Mayne A and Dujardin G 1997 *Phys. Rev. Lett.* **79** 2498
[30] Powers J M, Wander A, Rous P J, Van Hove M A and Somorjai G A 1991 *Phys. Rev.* B **44** 11159
[31] Long J P, Bermudez V M and Ramaker D E 1996 *Phys. Rev. Lett.* **76** 991
[32] Semond F 1996 *PhD Thesis* no 4680, Université de Paris-Sud/Orsay
[33] Derycke V, Soukiassian P, Mayne A, Dujardin G and Gautier J 1998 *Phys. Rev. Lett.* **81** 5868
[34] Derycke V, Soukiassian P, Mayne A and Dujardin G 2000 *Surf. Sci. Lett.* **446** L101
[35] Soukiassian P, Aristov V Yu, Douillard L, Semond F, Mayne A, Dujardin G, Pizzagalli L, Joachim C, Delley B and Wimmer E 1999 *Phys. Rev. Lett.* **82** 3721
[36] Douillard L, Aristov V Yu, Semond F and Soukiassian P 1998 *Surf. Sci. Lett.* **401** L395
[37] Yeom H W, Shimomura M, Kitamura J, Hara S, Tono K, Matsuda I, Mun B S, Huff W A R, Kono S, Ohta T, Yoshida S, Okuski H, Kajimura K and Fadley C S 1999 *Phys. Rev. Lett.* **83** 1640
[38] Aristov V Yu, Douillard L, Fauchoux O and Soukiassian P 1997 *Phys. Rev. Lett.* **79** 3700
[39] Yan H, Smith A P and Jónsson H 1995 *Surf. Sci.* **330** 265
[40] Sabisch M, Krüger P, Mazur A, Rohlfing M and Pollmann J 1996 *Phys. Rev.* B **53** 13121
[41] Käckell P, Furthmüller J, Bechstedt F, Kresse G and Hafner J 1996 *Phys. Rev.* B **54** 10304
[42] Catellani A, Galli G and Gygi F 1996 *Phys. Rev. Lett.* **77** 5090
[43] Catellani A, Galli G, Gygi F and Pellacini F 1998 *Phys. Rev.* B **57** 12255
[44] Douillard L, Semond F, Aristov V Yu, Soukiassian P, Delley B, Mayne A, Dujardin G and Wimmer E 1998 *Silicon Carbide and III–V Nitrides and Related Materials* (*Materials Science Forum* vol 264) (Switzerland: TransTech) p 379
[45] Lu W, Krüger P and Pollmann J 1998 *Phys. Rev. Lett.* **81** 2292
[46] Derycke V 2000 *PhD Thesis* no 6304, Université de Paris-Sud/Orsay
[47] Bermudez V M 2003 *Nat. Mater.* **2** 21
[48] Aristov V Yu, Douillard L, Fauchoux O, Semond F and Soukiassian P 1997 *Omicron Newsletters* **IV** 4

[49] Aristov V Yu, Enriquez H, Derycke V, Soukiassian P, Le Lay G, Grupp C and Taleb-Ibrahimi A 1999 *Phys. Rev.* B **60** 16553
[50] D'angelo M, Enriquez H, Aristov V Yu, Soukiassian P, Renaud G, Barbier A, Noblet M, Chiang S and Semond F 2003 *Phys. Rev.* B **68** 165321
[51] Riehl-Chudoba M, Soukiassian P, Jaussaud C and Dupont S 1995 *Phys. Rev.* B **51** 14300
[52] Soukiassian P 1999 *Mater. Sci. Eng.* B **61** 506
[53] Hara S, Slijkerman W F J, van der Veen J F, Ohdomari I, Misawa S, Sakuma E and Yoshida S 1990 *Surf. Sci. Lett.* **231** L196
[54] Yoshinobu T, Izumikawa I, Mitsui H, Fuyuki T and Matsunami H 1991 *Appl. Phys. Lett.* **59** 2844
[55] Dayan M 1985 *J. Vac. Sci. Technol.* A **3** 361
[56] Dayan M 1986 *J. Vac. Sci. Technol.* A **4** 38
[57] Hara S, Misawa S, Yoshida S and Aoyagi Y 1994 *Phys. Rev.* B **50** 4548
[58] Yeom H W, Chao Y C, Terada S, Hara S, Yoshida S and Uhrberg R I G 1997 *Phys. Rev.* B **56** R15525
[59] Yeom H W, Chao Y C, Matsuda I, Hara S, Yoshida S and Uhrberg R I G 1998 *Phys. Rev.* B **58** 10540
[60] Lübbe M, Lindner K, Sloboshanin S, Tautz S, Schafer J and Zahn D R T 1998 *J. Vac. Sci. Technol.* A **16** 3741
[61] Pizzagalli L, Catellani A, Galli G, Gygi F and Baratoff A 1999 *Phys. Rev.* B **60** R5129
[62] Lu W C, Krüger P and Pollmann J 1999 *Phys. Rev.* B **60** 2495
[63] Shevlin S A and Fisher A J 2000 *Phys. Rev.* B **62** 6904
[64] Yeom H W, Matsuda I, Chao Y C, Hara S, Yoshida S, Kajimura K and Uhrberg R I G 2000 *Phys. Rev.* B **61** R2417
[65] Derycke V, Soukiassian P, Amy F, Chabal Y, D'angelo M, Enriquez H and Silly M 2003 *Nat. Mater.* **2** 253
[66] Rossow U, Lindner K, Lübbe M, Aspnes D E and Zhan D R T 1998 *J. Vac. Sci. Technol.* B **16** 2355
[67] Lu W C, Schmidt W G, Briggs E L and Bernholc J 2000 *Phys. Rev. Lett.* **85** 4381
[68] Renaud G 1998 *Surf. Sci. Rep.* **32** 1–90
[69] Feidenhans'l R 1989 *Surf. Sci. Rep.* **10** 105–88
[70] Robinson I K and Tweet D J 1992 *Rep. Prog. Phys.* **55** 599
[71] Amy F, Enriquez H, Soukiassian P, Storino P F, Chabal Y J, Mayne A J, Dujardin G, Hwu Y K and Brylinski C 2001 *Phys. Rev. Lett.* **86** 4342
[72] Amy F, Soukiassian P, Hwu Y K and Brylinski C 2002 *Phys. Rev.* B **65** 165323
[73] Bermudez V M and Long J P 1995 *Appl. Phys. Lett.* **66** 475
[74] Shek M L 1996 *Surf. Sci.* **349** 317
[75] Douillard L, Fauchoux O, Aristov V Yu and Soukiassian P 2000 *Appl. Surf. Sci.* **166** 220
[76] Derycke V, Fonteneau P and Soukiassian P 2000 *Phys. Rev.* B **62** 12660
[77] Douillard L, Fauchoux O, Aristov V Yu and Soukiassian P 2000 *Appl. Surf. Sci.* **166** 220
[78] Semond F, Soukiassian P, Mangat P S and di Cioccio L 1995 *J. Vac. Sci. Technol.* B **13** 1591
[79] Semond F, Soukiassian P, Mangat P S, Hurych Z, di Cioccio L and Jaussaud C 1996 *Appl. Surf. Sci.* **104** 79
[80] Soukiassian P 1998 *Fundamental Aspects of Ultrathin Dielectrics on Si-Based Devices: Towards an Atomic Scale Understanding* (*NATO ASI Series*) ed E Garfunkel, E P Gusev and A Ya Vul' (Dordrecht: Kluwer) p 257
[81] Semond F, Douillard L, Soukiassian P, Dunham D, Amy F and Rivillon S 1996 *Appl. Phys. Lett.* **68** 2144
[82] Dunham D, Mehlberg S, Chamberlin S, Soukiassian P, Denlinger J D, Rotenberg E, Tonner B and Hurych Z D 2003 *J. Vac. Sci. Technol.* B **21** 1876
[83] Enriquez H, Derycke V, Aristov V Yu, Soukiassian P, Le Lay G, Cricenti A, Crotti C, Ferrari L and Perfetti P 2000 *Appl. Surf. Sci.* **162** 559
[84] Whitman L J, Stroscio J A, Dragoset R A and Celotta R J 1991 *Science* **251** 1206
[85] Shen T C, Wang C, Abaln G C, Tacker J R, Lyding J W, Avouris Ph and Walkup R E 1995 *Science* **268** 1590
[86] Soukiassian L, Mayne A J, Carbone M and Dujardin G 2003 *Phys. Rev.* B **68** 035303
[87] 1999 Nanotechnology Research Directions: Vision for Nanotechnology R&D in the Next Decade, National Science and Technology Council, The White House, Washington, September
[88] Aristov V Yu, Douillard L and Soukiassian P 1999 *Surf. Sci. Lett.* **440** L285
[89] Derycke V, Pham N P, Fonteneau P, Soukiassian P, Aboulet-Nze P, Monteil Y, Mayne A J, Dujardin G and Gautier J 2000 *Appl. Surf. Sci.* **162** 413
[90] Soukiassian P 2001 *Physics, Chemistry and Application of Nanostructures* (Singapore: World Scientific) p 340
[91] Lu W, Krüger P and Pollmann J 2000 *Phys. Rev.* B **61** 2680
[92] Catellani A, Galli G and Rigolli P L 2000 *Phys. Rev.* B **62** R4794
[93] Higashi G S and Chabal Y J 1993 *Handbook of Silicon Wafer Cleaning Technology: Science, Technology and Applications* ed W Kern (Park Ridge, NJ: Noyes) p 433

[94] Oura K, Lifshits V G, Saranin A A, Zotov A V and Katayama M 1999 *Surf. Sci. Rep.* **35** 1
[95] Derycke V, Fonteneau P, Pham N P and Soukiassian P 2001 *Phys. Rev.* B **63** R201305 (rapid communication)
[96] Kratzer P, Pehlke E, Scheffler M, Rascke M B and Höfer U 1998 *Phys. Rev. Lett.* **81** 5596 and references therein
[97] Widstrand S M, Johansson L S O, Magnusson K O, Larsson M I, Yeom H W, Hara S and Yoshida S 2001 *Surf. Sci.* **479** 247
[98] D'angelo M 2003 *PhD Thesis* no 7247, Université de Paris-Sud/Orsay
[99] D'angelo M, Enriquez H, Silly M G, Derycke V, Aristov V Yu, Soukiassian P, Ottaviani C, Pedio M and Perfetti P 2004 *Materials Science Forum* (Switzerland: TransTech) at press
[100] Wilson M 2003 Search and Discovery *Phys. Today* **56** 18
[101] Tsugawa K, Kitatani K, Noda H, Hokazono A, Tajima M and Kawarada H 1999 *Diamond Relat. Mater.* **8** 927
[102] Maier F, Riedel M, Mantel B, Ristein J and Ley L 2000 *Phys. Rev. Lett.* **85** 3472
[103] Teukam Z, Chevallier J, Saguy C, Kalish R, Ballutaud D, Barbé M, Jomard F, Tromson-Carli A, Cyterman C, Butler J E, Bernard M, Baron C and Deneuville A 2003 *Nat. Mater.* **2** 482